Department of Aerospace Science and Technology
Master of Science in Space Engineering

POLITECNICO
MILANO 1863

Optimal guidance strategy for active debris removal of a tumbling object

Supervisor:
Prof.ssa Camilla Colombo

Co-Supervisor:
Giacomo Borelli

Candidate:
Marco Gonella

Student ID:
913381

Academic Year 2021-2022

Acknowledgements

Questo elaborato rappresenta il coronamento di anni di studio e formazione personale in cui muovo i primi passi nel meraviglioso mondo della teoria del controllo; perciò, devo ringraziare la professoressa Camilla Colombo e il correlatore Giacomo Borelli per l'opportunità fornitami, l'estrema disponibilità e competenza, l'enorme pazienza e la saggezza nell'indirizzare lo sviluppo di questa tesi. Detto questo prima di addentrarsi nei dettagli del lavoro ritengo sia doveroso profondersi in più che dovuti ringraziamenti agli amici, fuori e dentro l'università, e alla famiglia.

Grazie al "Branco" e a tutti i suoi elementi per esserci ancora nonostante tutte le avventure e disavventure vissute: Grazie ad Achi, a Garba, a Giulio, al Pocho e al Deste, che purtroppo l'anno scorso ci ha lasciati, per avere la fortuna di potervi considerare degli amici autentici, quelli che sono presenti a discapito di impegni e interessi personali e a cui qui nessuna parola scritta o pensiero potrebbero mai rendere sufficiente giustizia specialmente ripensando ad alcune serate leggendarie. Grazie anche a Ricky per aver mantenuto un rapporto di sincera amicizia nonostante le separazioni scolastiche e lavorative.

Grazie agli amici dell'università. A quelli della triennale: Giorgio e Pachoc per aver condiviso l'emozione dell'avventura universitaria e gli interminabili rientri in treno, Bruco e Buffo per le ore trascorse in aula tra il serio e il faceto. A quelli della magistrale: Ale Bocci, compagno e veterano di innumerevoli progetti, Ale Guerra per lo spirito e l'efficienza, la Susy per l'immancabile supporto logistico, la Marty per la tenacia nello studio prima degli esami, il Team Argo per la profonda passione e coesione.

Non rimane ora che la famiglia per cui nessun ringraziamento sarebbe minimamente adeguato: A mio padre, instancabile mentore e modello a cui devo tutto ciò che sono. A mia madre, la cui costante presenza e l'incondizionato sostegno la rendono il pilastro portante della famiglia. Infine, annoverato per ultimo ma il più importante tra le persone che mi sono veramente care, mio fratello Michele a cui non posso che rendere omaggio per aver attraversato assieme l'intero percorso di crescita personale e scolastica, ma soprattutto per l'infinita capacità di sopportazione dimostrata in questi venti anni allietando ogni singolo giorno, specie quelli più oscuri, con umorismo di ineguagliabile sottigliezza.

Abstract

Space debris is becoming a severe issue threatening space activity and the space community is developing new technologies and methodologies to efficiently face the problem through missions of active debris removal. However the status of every singles debris requires an ad hoc solution: depending on size, mass and rotational states, several safety criteria must be introduced to avoid collision during the rendezvous phase of a removal mission.

These issues are addressed in this thesis. Starting from data from several databasess, the first part presents a general overview of the orbital collocation of debris, relating the orbital parameters to their attitude status. Then Envisat is chosen as the representative of this mission.

This work develops an optimal open-loop guidance trajectory for a safe synchronisation with uncooperative tumbling debris based on an impulsive scheme designed to reduce fuel consumption using quadratic criteria.

To test the feasibility of the guidance strategy and exploit efficiency, several preliminary simulations are performed to validate the control followed by Monte Carlo simulations aimed to find what configuration of initial conditions and time needed to perform the manoeuvre provide the cheapest synchronisation.

Sommario

I detriti spaziali stanno diventando un grave problema che minaccia l'attività spaziale e la comunità spaziale sta sviluppando nuove tecnologie e metodologie per affrontare in modo efficiente il problema attraverso missioni di rimozione attiva dei detriti. Tuttavia lo stato di ogni singolo detriti richiede una soluzione ad hoc: a seconda delle dimensioni, della massa e degli stati di rotazione, devono essere introdotti diversi criteri di sicurezza per evitare collisioni durante la fase di rendez-vous di una missione di rimozione.

Questi problemi sono affrontati in questa tesi. Partendo dai dati provenienti da diversi databases, la prima parte presenta una panoramica generale della collocazione orbitale dei detriti, mettendo in relazione i parametri orbitali con il loro stato di assetto. Quindi Envisat viene scelto come rappresentante di questa missione.

Questo lavoro sviluppa una traiettoria di guida ottimale ad anello aperto per una sincronizzazione sicura con detriti rotanti non cooperativi basata su uno schema impulsivo volto a ridurre il consumo di carburante utilizzando criteri quadratici.

Per testare la fattibilità della strategia di guida e sfruttarne l'efficienza, vengono eseguite diverse simulazioni preliminari per convalidare il controllo, seguite da simulazioni Monte Carlo volte a trovare quale configurazione delle condizioni iniziali e del tempo necessario per eseguire la manovra fornisca la sincronizzazione più economica.

List of acronyms

ADR	Active Debris Removal
CW	Clohessy–Wiltshire
ECI	Earth Centered Inertial
FOV	Field Of View
GNC	Guidance Navigation and Control
LEO	Low Earth Orbit
LQR	Linear Quadratic Regulator
LVLH	Local Vertical Local Horizontal
MPC	Model Predictive Control
QCQP	Quadratically Constrained Quadratic Programming
ROE	Relative Orbital Elements

List of Symbols

$\boldsymbol{\delta\alpha}$	Vector of relative orbital elements
$\boldsymbol{\omega}$	Vector of target's angular velocity
$\boldsymbol{q}_{B/N}$	Target attitude quaternion
$\boldsymbol{R}_{B/N}$	Target attitude matrix
μ	Earth's gravitational parameter
n	Orbital mean motion

Indice

Elenco delle tabelle

Elenco delle figure

Capitolo 1

Introduction

1.1 Overview of active debris removal activities

As a result of 70 years of space activities, the increase of space debris is potentially threatening nowadays activities requiring mitigation actions. The remarkable risk of collisions of the space debris with the operational satellites has been proven in early 2009 with the collision of the Iridium-33 satellite with the decommissioned Cosmos-2251 spacecraft. To this aim in the last decades, several studies have been performed to assess the feasibility of a mission able to remove the most problematic debris in order to prevent collisions and further fragmentation:

In [7] the authors explore all the most critical issues concerning feasible Active Debris Removal (ADR) mission, in particular focusing in the high level requirements depending on the number of debris to be removed and their size. The process of selection of a target to be removed is nontrivial and concern the debris nature, the re-entry capability, the safety priority and the national responsibility in order to grant an efficient stabilisation of the orbital environment.

In [33] the authors present a possible chaser system and the Guidance Navigation and Control (GNC) architecture for the e.Deorbit mission phase B1 aimed to capture the uncooperative target satellite Envisat. The operation considered span from ascent from launch orbit to the target orbit, rendezvous with the target satellite, capture and stabilisation of the coupled system and de-orbiting. So the study focus on the detail

of the capture procedure and the necessary instrumentation for an effective and precise attitude determination, mostly based on navigation camera. Particular care is devoted to the approach and rendez-vous trajectories, providing a passively safe approach until the proximity operations begin, where the chaser has to synchronise its motion with the target due to its large dimensions. For both synchronisation on the capture phases, the control system is based on feedback linearization to cancel the centrifugal terms allowing for precise station keeping during the critical capture phase by means of a robotic arm.

In [37] the authors show a detailed characterisation of the Guidance Navigation and Control (GNC) scenario with the multiple phases the chaser has to face providing insight on several approach strategies. In particular several possible challenges are analysed providing the GNC strategies and scenarios, characterised by a combination of reliable and practical technologies, leading so to lower economical thresholds for ADR missions. Among the solution proposed there are: the adoption of infrared camera navigation and an angles-only navigation to makes the relative navigation reliable in the case the target does not have dedicated markers and retro reflectors. The detumbling by plume impingement when the target is rotating too fast for the ADR spacecraft to make a safe relative motion synchronisation with the target's rotation and complete mechanical capture. A dedicated relative navigation sensor and docking mechanism for payload attachment fitting of the target for those debris lacking a dedicated docking mechanism. Finally in the deorbit phase: a combined utilisation of efficient electric propulsion system and atmospheric drag to lower the altitude of the heavy target reducing the fuel cost of the ADR satellite, a minimum delta-V reentry manoeuvre using atmospheric drag to lower as much as possible the fuel consumption of the high-thrust propulsion system needed to perform controlled reentry.

In [28] the authors present a survey of methods for active debris removal, where the various concepts and methods are classified into laser-based, ion-beam shepherd-based, tether-based, sail-based, satellite-based, unconventional, and dynamical systems-based methods. The laser-based ADR concept involves high-power laser used to sublimate the debris, either from ground or space. Instead the ion-beam shepherd concept requires the

emission of a beam of quasi-neutral plasma toward a target to impart a propulsive force on it, but with the system operating only in close-range due to beam divergence effects and pointing errors. The tether-based ADR concept involves attaching a long wire to a piece of debris and letting the Earth's magnetic field act on it to slowly pull it back into the atmosphere, requiring an adaptive control strategy for harpooning, flexible tethered-net deployment, net closing mechanism, low-work function tethers, and hybrid tension control method. The sail-based method involves using a large surface fabric to trap the solar radiation pressure and use it as a method of propulsion or control, with the paper analysing the sail's deorbit time, the deployable drag sail and the inflatable magnetic sail. The concept of satellite-based ADR method involved a rigid capture of the target by means of a robotic arm mounted on the chaser; the main technological difficulties are associated with the kinematics coupling between the robotic arm and the uncooperative target, in order to grant the safety and efficiency of the manoeuvre.

A complete ADR mission consist of several phases:

- Ground-based observation campaign, for optical and radar observations from the ground to collect as much information as possible about the attitude motion of the target.
- Orbital injection, with the rocket launched toward the target and the consequential ADR spacecraft separation into the orbital height and orbital plane appropriate for rendezvous to the target.
- Homing far rendezvous, with two candidate approach for the relative orbit [32]: spiral orbit and v-bar hopping. Although the passive abort trajectories of these relative orbits are both safe, the spiral orbit is more robust than the V-bar hopping against collisions. On the other hand, the V-bar hopping is a relative orbit closer to a straight line, making it easy to design the attitude of the ADR spacecraft and the field of view of the relative navigation sensor.

- Inspection phase to perform pose estimation of the target and observe the physical features.
- Preliminary target contactless detumbling if needed, followed by close rendezvous approach, with possible angular synchronisation toward the docking position subject to collision avoidance constraints for safety.
- Final docking by means of rigid capture during station keeping.
- Debris orbit lowering and/or reentry, using the minimum delta-V reentry method exploiting air drag to control the reentry to Earth's surface with a small amount of propellant and small thrust [37].

1.2 Control method review

In the context of an ADR mission the rendezvous scenario becomes the most critical part due to safety reasons, especially in the case of uncooperative tumbling debris: the target is required to avoid catastrophic collisions potentially leading to debris increase. The rendezvous phase has been studied in the context of relative orbital dynamics and the problem consist in guiding the chaser along a path toward to a selected docking position but avoiding at the same time the collision with the target.

The whole problem is nontrivial and nonlinear and in the optics of practical implementation of a guidance scheme many simplifications are introduced:

- Partial or full decoupling between the translational and rotational dynamics of the chaser.
- Linearisation of the chaser orbital motion around the target orbit formalised or in cartesian coordinate, leading to Clohessy–Wiltshire (CW) equations [2], or in Relative Orbital Elements (ROE) [15] for a more accurate relative motion.
- Introduction of geometric criteria to impose the safety which drive the nature of the optimisation of the control problem.

To tackle the problem several guidance philosophies have been used, among which artificial potential, inverse dynamics, impulsive guidance, programming methods, with the control counterpart for the reference tracking: feedback linearisation, Lyapunov control function and suitably for linear systems, Linear Quadratic Regulator (LQR) or Model Predictive Control (MPC) in the presence of constraints.

Concerning artificial potential, the guidance trajectory is obtained via the sum of attractive and repulsive potentials. The attractive potential typically is defined as quadratic to ensure a global minimum, while the repulsive one is constructed as exponential of a function describing the contour of keep out regions [6], to ensure a rapid decay away from obstacle and so lowering the repulsive control action. To follow the reference trajectory the control is imposed via Lyapunov control function method and in order to increase optimality LQR is used in case of linear system, or by an adaptive potential also via Lyapunov theory [38].

Inverse Dynamics takes advantage of an analytical solution to the axis-symmetric tumbling case to simply model the motion of the docking port, simplifying attitude propagation. With the imposition of the trajectory and the attitude by means of polynomials [10], the optimality is obtained minimising the fuel cost based on force computation by minimising over the polynomial coefficient representing the dynamics [19]. The open-loop trajectory guidance results in nonlinear constrained programming with path constraint including sensor Field Of View (FOV) constraints [34]. In all works to generate closed loop guidance scheme, the trajectory is repeatedly adjusted at a certain frequency based on the current state of both chaser and target.

Impulsive techniques are based on the discretisation of the dynamics leading to finite dimension programming problem [9][17], where usually the fuel cost function requires the minimisation of the one norm with respect to the classical quadratic energetic cost [20].

1.3 Scope of the thesis

The purpose of this work is to study an optimal fuel reduction scheme through impulsive control to generate an open-loop optimal trajectory for the close proximity operations.

Specifically, the work focuses on the synchronisation phases where the chaser from a characterisation relative orbit is supposed to reach the docking position with respect to an uncooperative tumbling target. To enable the safe apporach to the uncontrolled rotating debris, specific constraints and strategies have been explored in this work.

1.4 Thesis outline

This thesis work is organised as follows:

- Chapter 2 deals with the scenario selection for the synchronisation phase of an ADR mission, based on statistical consideration from various satellites' orbits and attitude catalogues.
- Chapter 3 describes the mathematical formulation of the problem based on relative orbital elements.
- Chapter 4 presents the description of the adopted control method from optimal control theory to impulse control.
- Chapter 5 presents the test cases validation starting from real satellite data and results obtained through the numerical simulation.
- Chapter 6 summarises the final considerations and conclusions on the obtained results and possible extensions in future works.

Capitolo 2

Debris population analysis

2.1 Active debris removal

To successfully achieve an ADR mission great attention has to be given to the scenario selection for the target satellite. The literature is plenty of risks/benefits analyses in which some criteria drive the candidate target selection [7]: orbital slot, collision probability and commercial interests just to name a few. Another relevant aspect affecting the mission is the attitude dynamical status of the target since as the angular rate grows in magnitude, the close proximity manoeuvres become riskier and more fuel costly. To cope with these aspects is necessary to assess the rotational dynamics of the target to correctly set up the approach logic. Based on the ESA DISCOS catalogue [23], CelesTrak TLE data [11] and MMT telescope lightcurve database [31] a preliminary simple but effective statistic baseline is built to rationally set the case study relating the coupling between geometry, attitude, orbital motion and mass.

2.2 Angular regime assessment

Since this work focuses on synchronisation, it is important to define the angular regime of the target in order to properly select the case. Figure 2.1 provide the angular rate distribution among satellites and rocket bodies population making a distinction based on three angular rate regimes: aperiodic, non-variable and periodic.

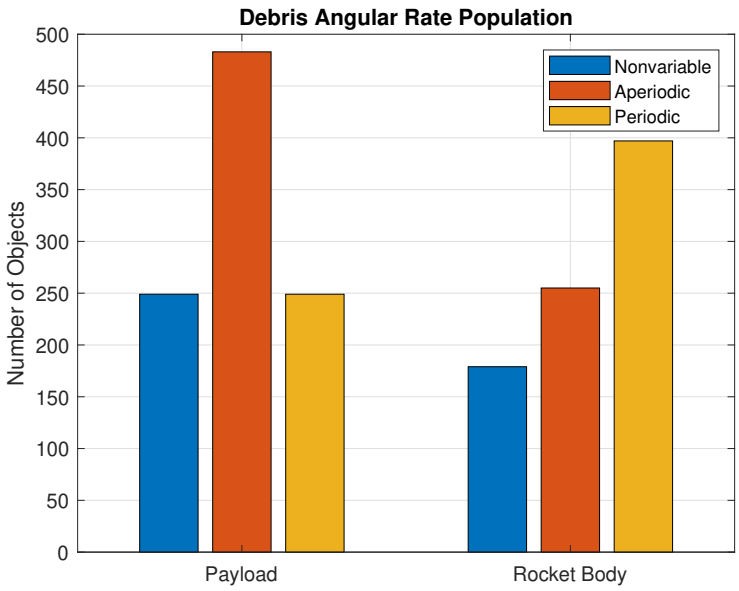

Figura 2.1: Angular rate population.

It can be seen that satellites are mainly subject to aperiodic variation more than for rocket bodies mainly caused by lower geometric symmetry due to solar panels and various appendages, which makes the body more sensitive to disturbance torques such as gravity gradient, solar radiation pressure, Earth magnetic field etc. Instead, a synchronisation manoeuvre in the case of a periodic angular regime is a quite complex task for an autonomous rendezvous requiring high fuel cost and very constraining requirements from safety. Especially for fast rotators, the collision risk is much more severe and several structural issues concerning rigid capture arise in the next grasping phase. However for the close proximity phase of this work only target periodic angular regimes are considered.

2.3 Shapes

Starting from geometry a primary distinction has to be made dividing the debris into two classes, namely satellites and rocket bodies such as upper stages. The latter ones show a more regular shape due to axial-symmetric geometry which makes the angular motion more regular and from a safety perspective the absence of appendages makes the approach and capture of the tumbling safer than in the case of satellites.

Focusing on the inactive satellites, Figure 2.2 shows that the higher number is composed by box or prismatic main body plus an even number of panels/appendages.

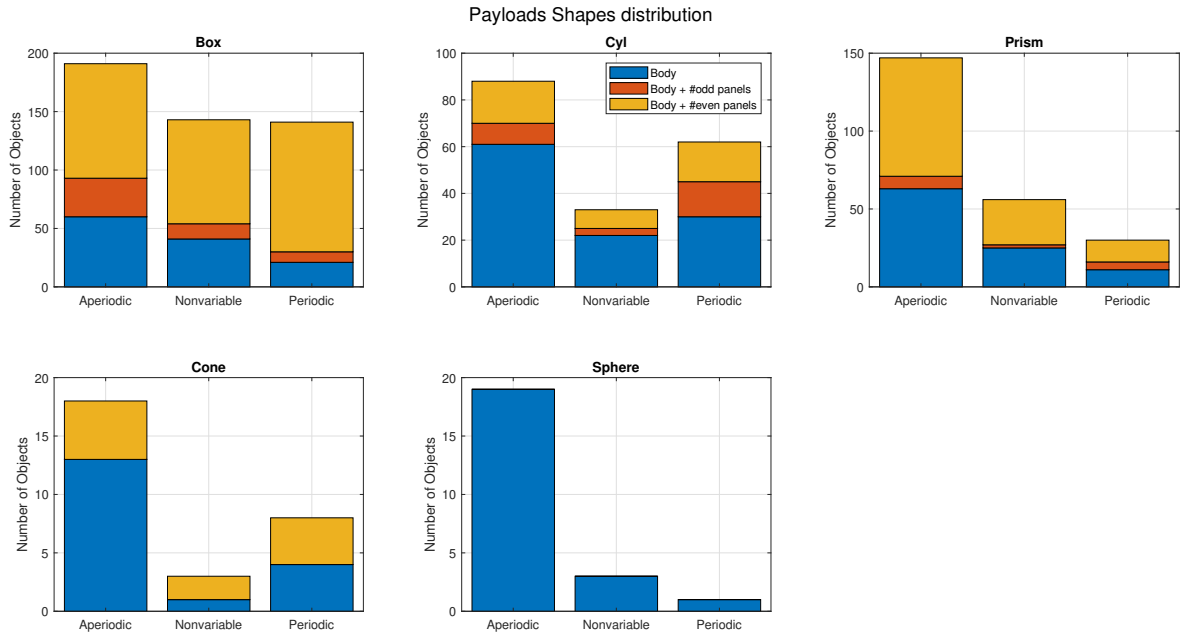

Figura 2.2: Payloads shapes distribution.

2.4 Orbital/attitude parameters statistics

Concerning the orbital collocation, Figure 2.3 and Figure 2.4 describe respectively the orbital slot in terms of the semi-major axis and inclination of the three angular rate regimes for the rocket body class and the satellite one.

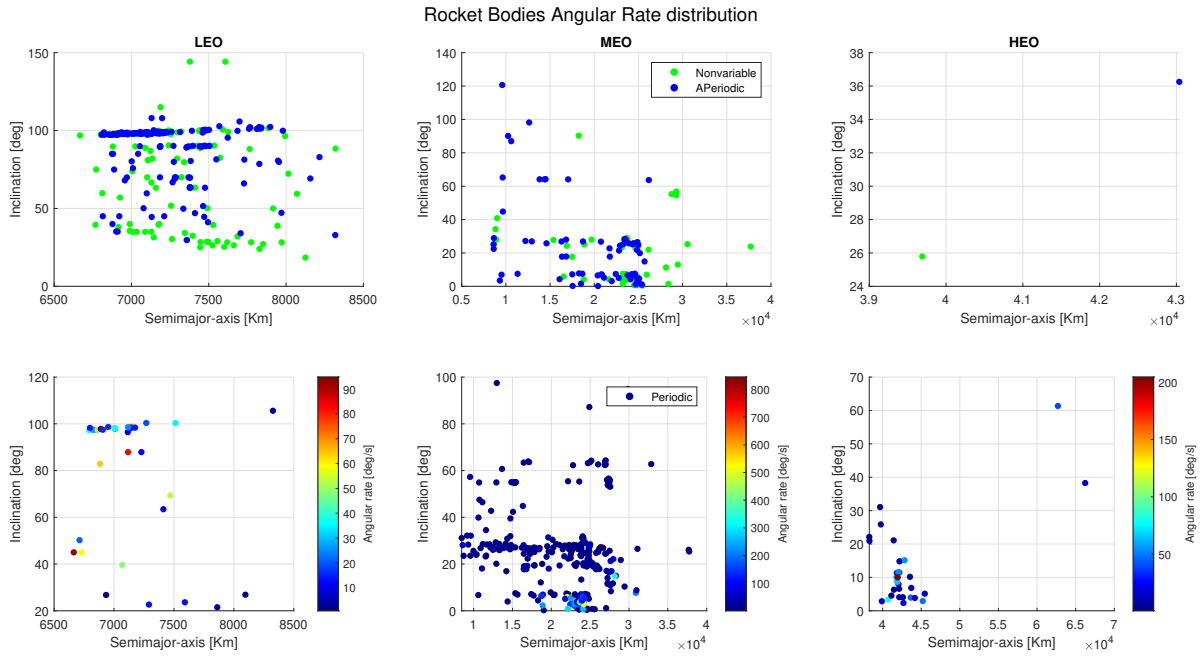

Figura 2.3: Rocket bodies angular rate distribution.

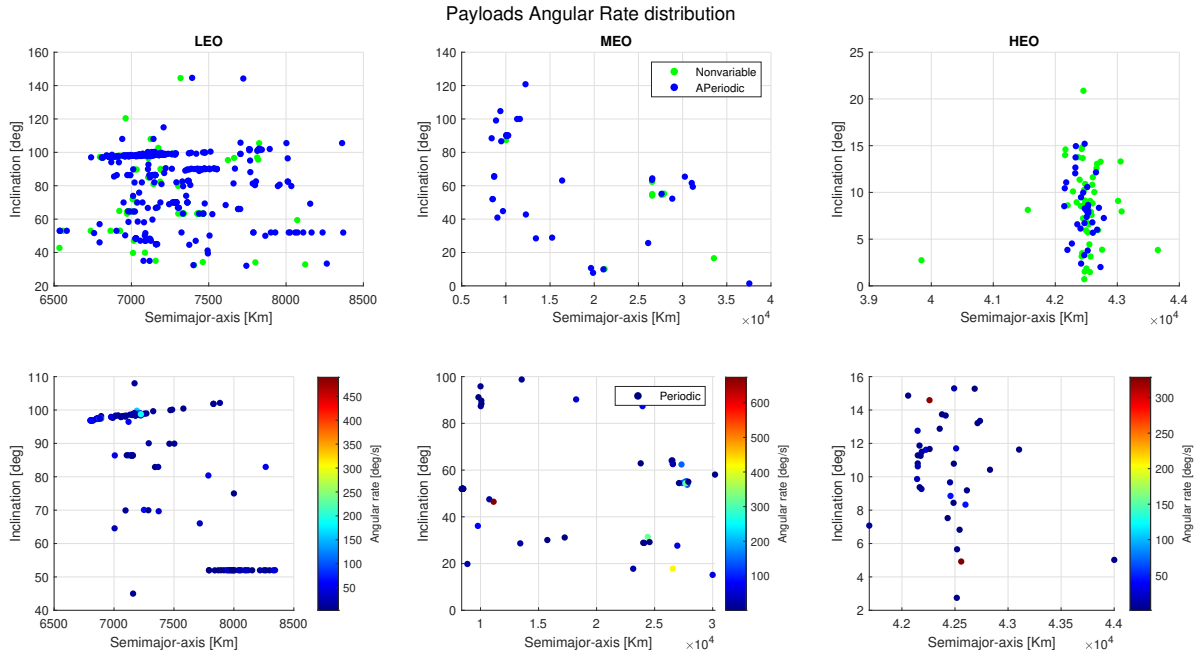

Figura 2.4: Payloads angular rate distribution.

For both Figures 2.2 and 2.3, the first three plots concern those ones established from the light curves (non-variable and aperiodic), while the ones below refer to the rotators. It is evident that concerning Low Earth Orbit (LEO), periodic rotators both fast and

slow tend to group around 50°and 98°-100°of Sun-synchronous and polar orbit especially in the case of rocket body. Focusing on LEO orbital region, being the most crowded one, Figure 2.5 and Figure 2.6 present the distributions of the Rocket bodies and payloads in terms of altitude, inclination, eccentricity and mass. In the second rows of the plots an estimation of the risk of collision is introduced, taking advantage of the probability function defined in [30], which is a monomial function depending on the debris lifetime, mass and fragmentation status.

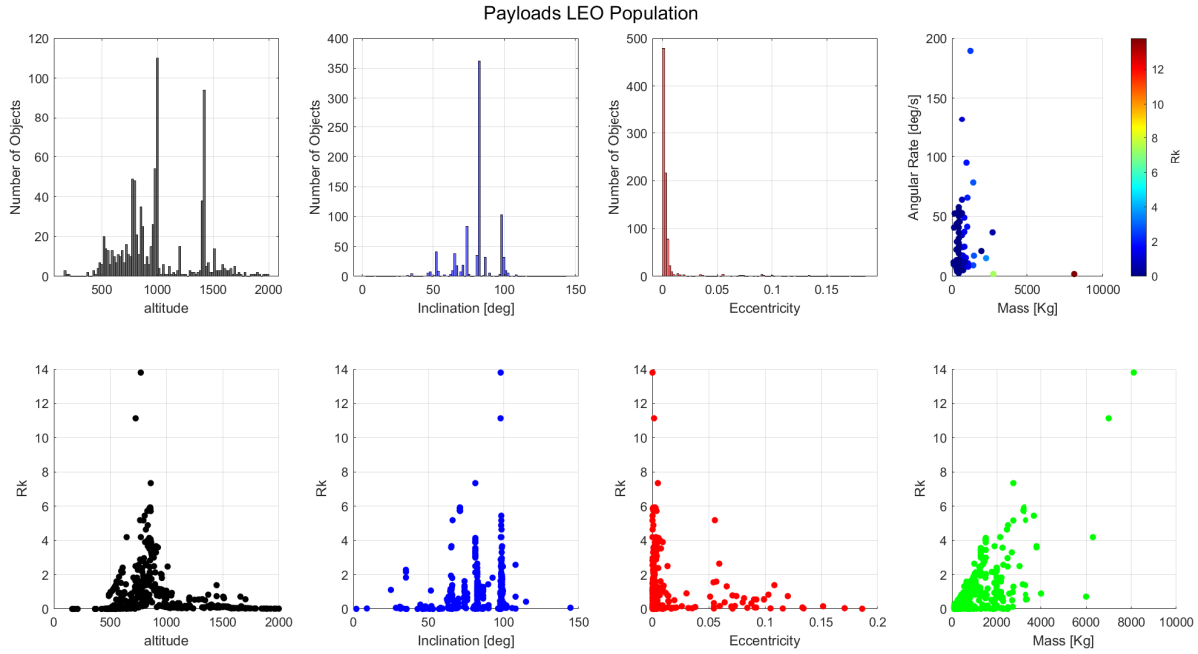

Figura 2.5: Payloads LEO population.

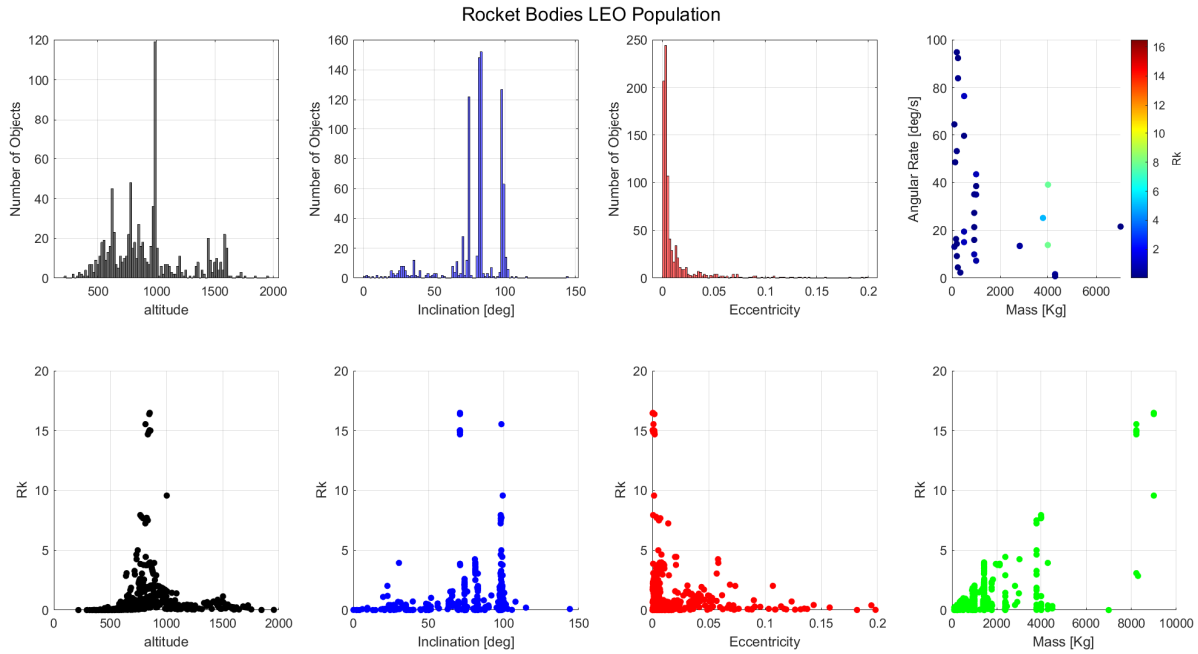

Figura 2.6: Rocket bodies LEO population.

In Figure 2.5, the payload population group around orbits characterised by an altitude between 500-1000 km, an inclination between 70°-80°and low values of eccentricity. However the payloads having highest collision risk lie in near-circular orbits around 100°of inclination. The rocket body population as visible in Figure 2.5, shares some common features with the payloads, namely the same distribution and risk level in the previous altitude range and very low eccentric orbit. Instead, concerning orbit inclination, it is visible an equal distribution in both numbers of objects and risk in the range 70°-100°.

2.5 Target selection

Summing up the analyses of the previous sections, the candidate debris case study belongs to the polar/Sun-synchronous orbit in LEO due to the fact that this orbital slot is the major representative of the riskiest debris. Moreover is considered debris having periodic angular behaviour but not necessarily gravity gradient stabilized in order to study the synchronisation motion with an uncooperative target while avoiding all the difficulties of the aperiodic angular regime. A natural target selection is Envisat, an ESA defunct satellite, for two main reasons: the first is the amount of works presented in the literature

devoted to correctly set up a real removal mission [1][5][16]. The other is due to the geometrical shape of the satellite which shares common features between the payloads and rocket body, so being a hybrid representative of this two categories.

Capitolo 3

Problem formulation

In this chapter, it is introduced the theoretical framework in which is formalised the control problem for the synchronisation of the chaser spacecraft with a tumbling target. In particular the chaser is required to match the position of the hold point, a fixed geometric position with respect to the target and needed for the successive capture phase. However the manoeuvre, due to the tumbling of the target, requires safety criteria to avoid the risk of collisions; so geometric keep-out zones are introduced. Since the problem involves a coupling between translation and rotational dynamics it is convenient to set some reference systems.

3.1 Orbital mechanics

3.1.1 Reference frames

To properly describe the orbital motion here two cartesian reference frame are defined: the Earth-Centered-Inertial (ECI) and the Local Vertical Local horizontal (LVLH), both mathematically defined by means of an orthogonal basis given by three unit vectors. Starting from the ECI, it is a geocentric reference system with the unit vector $\boldsymbol{i}$ pointing in the direction of vernal equinox, the unit vector $\boldsymbol{k}$ orthogonal to the Earth ecliptic plane and finally the unit vector $\boldsymbol{j}$ completing the frame as can be seen in Figure 3.1.

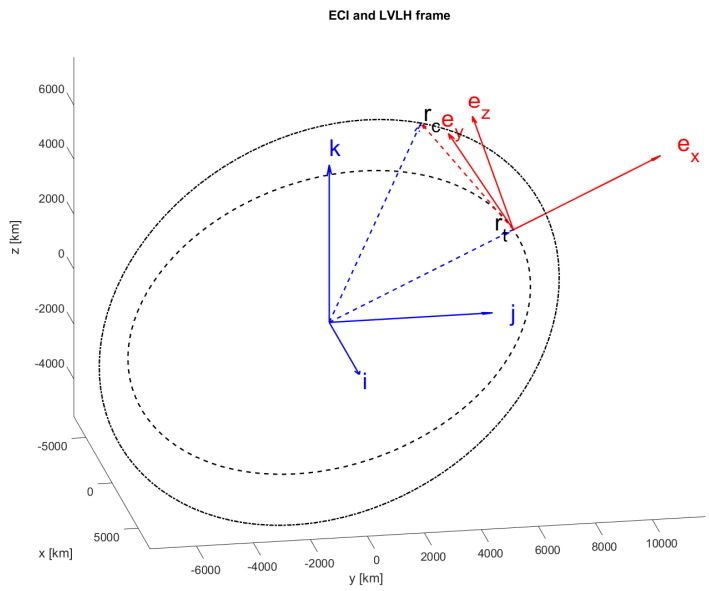

Figura 3.1: Reference sytems.

The second frame, Local Vertical Local Horizon (LVLH) is defined as a non-inertial frame with origin attached to the trajectory described by a point orbiting around Earth with the unit vector $\boldsymbol{e_x}$ in the radial direction, $\boldsymbol{e_z}$ in the direction of local angular momentum vector and finally the unit vector $\boldsymbol{e_y}$ completing the frame.

3.1.2 The relative orbital elements framework

The spacecraft orbital mechanics is well described by the Newtonian two body problem:

$$\ddot{\boldsymbol{r}} = -\mu \frac{\boldsymbol{r}}{\|\boldsymbol{r}\|^3} \tag{3.1.1}$$

in the hypothesis of spacecraft mass negligible with respect to the main attractor and symmetric gravitational potential, since here high order harmonics are not relevant for the derivation of the equations. It follows that the equations of motions of the target and the chaser are respectively:

$$\begin{cases} \ddot{\boldsymbol{r}}_t = -\mu \frac{\boldsymbol{r}_t}{\|\boldsymbol{r}_t\|^3} \\ \\ \ddot{\boldsymbol{r}}_c = -\mu \frac{\boldsymbol{r}_c}{\|\boldsymbol{r}_c\|^3} \end{cases} \tag{3.1.2}$$

Since the problem deals with relative motion, is worth defining the relative distance between chaser and target as $\boldsymbol{r}_{rel} = \boldsymbol{r}_c - \boldsymbol{r}_t$ and to insert this expression inside the equation of the chaser obtaining:

$$\ddot{\boldsymbol{r}}_{rel} = -\mu \frac{\boldsymbol{r}_{rel} + \boldsymbol{r}_t}{\|\boldsymbol{r}_{rel} + \boldsymbol{r}_t\|^3} + \mu \frac{\boldsymbol{r}_t}{\|\boldsymbol{r}_t\|^3} \tag{3.1.3}$$

As in relative mechanics, it is useful to change the reference system from ECI frame to LVLH adding the extra contribution terms related to noninertial frame and the system turns into:

$$\ddot{\boldsymbol{r}}_{rel} + \dot{\boldsymbol{\theta}} \wedge \boldsymbol{r}_{rel} + 2\boldsymbol{\theta} \wedge \dot{\boldsymbol{r}}_{rel} + \boldsymbol{\theta} \wedge \boldsymbol{\theta} \wedge \boldsymbol{r}_{rel} = -\mu \frac{\boldsymbol{r}_{rel} + \boldsymbol{r}_t}{\|\boldsymbol{r}_{rel} + \boldsymbol{r}_t\|^3} + \mu \frac{\boldsymbol{r}_t}{\|\boldsymbol{r}_t\|^3} \tag{3.1.4}$$

where $\wedge$ stands for the cross product. Due to the LVLH definition, now the target distance is along the x axis

$$\boldsymbol{r_t} = \begin{bmatrix} r_t \\ 0 \\ 0 \end{bmatrix} \tag{3.1.5}$$

while the target orbital angular velocity vector

$$\boldsymbol{\theta} = \begin{bmatrix} 0 \\ 0 \\ n \end{bmatrix} \tag{3.1.6}$$

is orthogonal to the trajectory and it can be assumed constant in the quasi-circular orbit case, with the orbit angular velocity.

$$n = \sqrt{\frac{\mu}{a^3}} \tag{3.1.7}$$

Considering now the first contribution in the right side of 3.1.2 the gravitational force admit the following first-order expansion:

$$\begin{cases} \boldsymbol{f} = \boldsymbol{g}\Big|_{\boldsymbol{r}_{rel}=0} + \boldsymbol{G}\Big|_{\boldsymbol{r}_{rel}=0} \boldsymbol{r}_{rel} \\ \boldsymbol{g} = -\mu \frac{\boldsymbol{r}_{rel}+\boldsymbol{r}_t}{\|\boldsymbol{r}_{rel}+\boldsymbol{r}_t\|^3} \\ \boldsymbol{G} = -mu \frac{1}{\|\boldsymbol{r}_{rel}+\boldsymbol{r}_t\|^3} (\boldsymbol{I} - 3\frac{(\boldsymbol{r}_{rel}+\boldsymbol{r}_t)(\boldsymbol{r}_{rel}+\boldsymbol{r}_t)^T}{\|\boldsymbol{r}_{rel}+\boldsymbol{r}_t\|^2}) \end{cases} \tag{3.1.8}$$

where the $\boldsymbol{G}$ is associated to the gravity gradient. Inserting the espressions developed in 3.1.8 into 3.1.2, allows the linearisation of the equations of motion leading to the so-called Clohessy–Wiltshire equations [2]:

$$\begin{cases} \ddot{x} - 2n\dot{y} + 3n^2 x = 0 \\ \ddot{y} + 2n\dot{x} = 0 \\ \ddot{z} + n^2 z = 0 \end{cases} \tag{3.1.9}$$

The equations system 3.1.9 admits an analytical solution [15]:

$$\begin{cases} x = a_1 - a_{34} \cos(nt - \phi) \\ y = a_2 - \frac{3nt}{2} a_1 + 2a_{34} \sin(nt - \phi) \\ z = +a_{56} \sin(nt - \theta) \\ v_x = +na_{34} \sin(nt - \phi) \\ v_y = -\frac{3n}{2} a_1 + 2na_{34} \cos(nt - \phi) \\ v_z = na_{56} \cos(nt - \theta) \end{cases} \tag{3.1.10}$$

where the a_j, $a_{ij} = \sqrt{a_i^2 + a_j^2}$ and the phases ϕ and θ are constants dependent on the initials conditions.

3.1.3 Relative Orbital Elements formulations

The ROE are defined as the difference between the orbital elements of the target and chaser [15]

$$\delta\boldsymbol{\alpha} = \begin{bmatrix} \delta a \\ \delta\lambda \\ \delta e_x \\ \delta e_y \\ \delta i_x \\ \delta i_y \end{bmatrix} = \begin{bmatrix} \frac{a_c - a_t}{a_c} \\ (M_c + \omega_c) + (M_t + \omega_t) - (\Omega_c - \Omega_t)\cos i_t \\ e_c \cos i_c - e_t \cos i_t \\ e_c \sin i_c - e_t \sin i_t \\ i_c - i_t \\ (\Omega_c - \Omega_t)\sin i_t \end{bmatrix} \tag{3.1.11}$$

where the subscript c stands for the chaser spacecraft whereas the subscript t for the target one. M is the mean anomaly, a the semi-major axis, e the eccentricity, i the orbit inclination, ω the argument of perigee and Ω the right ascension of the ascending node. The constants presented in the solution of the CW equations can be recast in the relative orbital elements following the work done by D'Amico [15] based on quasi-singular relative orbital elements by defining a proper map:

$$\boldsymbol{T}(t) = a_c \begin{bmatrix} 1 & 0 & -\cos(nt) & -\sin(nt) & 0 & 0 \\ 0 & 1 & +2\sin(nt) & -2\cos(nt) & 0 & 0 \\ 0 & 0 & 0 & 0 & \sin(nt) & -\cos(nt) \\ 0 & 0 & n\sin(nt) & -n\cos(nt) & 0 & 0 \\ -\frac{3n}{2} & 0 & +2n\cos(nt) & +2n\sin(nt) & 0 & 0 \\ 0 & 0 & 0 & 0 & n\cos(nt) & +n\sin(nt) \end{bmatrix} \tag{3.1.12}$$

$$\boldsymbol{x} = \boldsymbol{T}\delta\boldsymbol{\alpha} \tag{3.1.13}$$

This formulation is extremely useful since when perturbations are neglected the relative orbital elements reduce to a constant set apart the true anomaly which follows the Keplerian propagation. These constants provide a very important geometrical insight since they form the parameters of a general drifting ellipse where the out of plane motion, which is pure oscillatory, decouples from the in-plane one.

The natural evolution of the dynamic system can be described including also the $J2$ perturbation according to [24] as:

$$\delta\dot{\boldsymbol{\alpha}} = \boldsymbol{A}\delta\boldsymbol{\alpha} + \boldsymbol{B}\boldsymbol{u} \tag{3.1.14}$$

where $\boldsymbol{A}$ is the state matrix defined as:

$$\boldsymbol{A} = k\begin{bmatrix} 0 & 0 & 0 & 0 & 0 & 0 \\ -\frac{3n}{2k} - \frac{7}{2}EP & 0 & e_x GFP & e_y GFP & -FS & 0 \\ \frac{7}{2}e_y Q & 0 & -4e_x e_y GQ & -(1+4Ge_y^2)Q & 5e_y S & 0 \\ -\frac{7}{2}e_x Q & 0 & (1+4Ge_x^2)Q & 4e_x e_y GQ & -5e_x S & 0 \\ 0 & 0 & 0 & 0 & 0 & 0 \\ \frac{7}{2}S & 0 & -4e_x GS & -4e_y GS & 2T & 0 \end{bmatrix} \tag{3.1.15}$$

whereas $\boldsymbol{B}$ is the control input matrix, obtained starting from the Gauss variational equation and linearising around the target orbital element [12].

$$\boldsymbol{B} = \frac{1}{a_t n_t}\begin{bmatrix} \frac{2}{\eta}e_t \sin\nu_t & \frac{2}{\eta}(1+e_t\cos\nu_t) & 0 \\ -\frac{2\eta^2}{1+e_t\cos\nu_t} & 0 & 0 \\ \eta\sin(\omega_t+\nu_t) & \eta\frac{(2+e_t\cos\nu_t)\cos(\omega_t+\nu_t)+e_x}{1+e_t\cos\nu_t} & \frac{e_y}{\tan i_t}\frac{\sin(\omega_t+\nu_t)}{1+e_t\cos\nu_t} \\ -\eta\cos(\omega_t+\nu_t) & \eta\frac{(2+e_t\cos\nu_t)\sin(\omega_t+\nu_t)+e_y}{1+e_t\cos\nu_t} & -\frac{e_x}{\tan i_t}\frac{\sin(\omega_t+\nu_t)}{1+e_t\cos\nu_t} \\ 0 & 0 & \eta\frac{\cos(\omega_t+\nu_t)}{1+e_t\cos\nu_t} \\ 0 & 0 & \eta\frac{\sin(\omega_t+\nu_t)}{1+e_t\cos\nu_t} \end{bmatrix} \tag{3.1.16}$$

The symbols refers to:

$$\begin{cases} e_x = e_t \cos\omega_t \quad e_y = e_t \sin\omega_t \\ \eta = \sqrt{1-e_t^2} \\ \gamma = \frac{1}{2} J_2 (\frac{R_e}{a_t})^2 \frac{1}{\eta^4} \\ k = \frac{3\gamma n}{2} \\ E = 1+\eta \quad F = 4+3\eta \quad G = \frac{1}{\eta^2} \\ P = 3\cos {i_t}^2 - 1 \quad Q = 5\cos {i_t}^2 - 1 \\ S = \sin 2i_t \quad T = \sin {i_t}^2 \end{cases} \tag{3.1.17}$$

For the case of quasi circular target orbit reference ($e_t \approx 0$) the system reduces to

$$\boldsymbol{A} = \begin{bmatrix} 0 & 0 & 0 & 0 & 0 & 0 \\ -\frac{3n}{2} - \frac{21\gamma n}{2}(3\cos^2 i_t - 1) & 0 & 0 & 0 & -\frac{21\gamma n}{2}\sin 2i_t & 0 \\ 0 & 0 & 0 & -\frac{3\gamma n}{2}(5\cos^2 i_t - 1) & 0 & 0 \\ 0 & 0 & \frac{3\gamma n}{2}(5\cos^2 i_t - 1) & 0 & 0 & 0 \\ 0 & 0 & 0 & 0 & 0 & 0 \\ \frac{21\gamma n}{4}\sin 2i_t & 0 & 0 & 0 & 3\gamma n \sin {i_t}^2 & 0 \end{bmatrix} \tag{3.1.18}$$

and

$$\boldsymbol{B} = \frac{1}{a_t n_t} \begin{bmatrix} 0 & 2 & 0 \\ -2 & 0 & 0 \\ \sin u & 2\cos u & 0 \\ -\cos u & 2\sin u & 0 \\ 0 & 0 & \cos u \\ 0 & 0 & \sin u \end{bmatrix} \tag{3.1.19}$$

with

$$u = w_t + M_t + n(1 + \frac{3}{2}\gamma(\cos(i_t)^2(5+3\eta) + 1 - \eta))t \tag{3.1.20}$$

3.2 Attitude dynamics

3.2.1 Euler equations

To complete the problem formulation it is needed to be added also the rotational dynamics, which is described by the well known Euler rotational equation in the body frame [29]:

$$\boldsymbol{J}\dot{\boldsymbol{\omega}} + \boldsymbol{\omega} \wedge \boldsymbol{J}\boldsymbol{\omega} = \boldsymbol{T}_{gg} \tag{3.2.1}$$

where the $\boldsymbol{J}$ is the inertia matrix, $\boldsymbol{\omega}$ the angular rate vector while $\boldsymbol{T}_{gg}$ is the vector associated with the gravity gradient torque which is defined as

$$\boldsymbol{T}_{gg} = 3n^2\boldsymbol{\gamma} \wedge \boldsymbol{J}\boldsymbol{\gamma} \tag{3.2.2}$$

for the quasi-circular orbit and where the right hand side with

$$\boldsymbol{\gamma} = \boldsymbol{R}_{B/L} \begin{bmatrix} 1 \\ 0 \\ 0 \end{bmatrix} \tag{3.2.3}$$

is the first row of the attitude matrix $\boldsymbol{R}_{B/L}$, defined by Equation 3.2.2, mapping the LVLH frame into the body frame.

3.2.2 Attitude kinematics

The kinematic equation accounts for the attitude variation and is given by [29]:

$$\dot{\boldsymbol{R}}_{B/N} = -[\boldsymbol{\omega}]^{\wedge}\boldsymbol{R}_{B/N} \tag{3.2.4}$$

where $R_{B/N}$ is the attitude matrix mapping the inertial reference system N into the body frame B, and the $[\quad]^{\wedge}$ is the operator indicating the skew-symmetric matrix associated with the vector to which is applied.

However, since the equations of motion of the chaser are written in the LVLH frame it is better to rewrite the kinematic equation in terms of attitude error between LVLH and the body frame:

$$\dot{\boldsymbol{R}}_{B/L} = -[\boldsymbol{\omega}_{B/L}]^{\wedge}\boldsymbol{R}_{B/L} \tag{3.2.5}$$

where $\boldsymbol{R}_{B/L}$ is the attitude between LVLH and body frame while

$$\boldsymbol{\omega}_{B/L} = \boldsymbol{\omega} - \boldsymbol{R}_{B/L}\boldsymbol{\theta} \tag{3.2.6}$$

is the angular velocity error whose components are easily obtained using the difference between the body angular velocity and the orbital one projected in the body frame resulting in a nonlinear coupling in the kinematics equation.

To avoid singularities during the integration process, the attitude kinematics is reformulated using the quaternions formalism:

$$\boldsymbol{q} = \begin{bmatrix} q_x \\ q_y \\ q_z \\ q_w \end{bmatrix} \tag{3.2.7}$$

where $\boldsymbol{q}$ is a unitary four dimensional vector whose component are linked to the Euler axis/angle parameters [35].

So finally using the map:

$$\boldsymbol{R}_{B/L} = \begin{bmatrix} q_w^2 + q_x^2 - q_y^2 - q_z^2 & 2(q_x q_y + q_z q_w) & 2(q_x q_z - q_y q_w) \\ 2(q_x q_y - q_z q_w) & q_w^2 - q_x^2 + q_y^2 - q_z^2 & 2(q_y q_z + q_x q_w) \\ 2(q_x q_z + q_y q_w) & 2(q_y q_z - q_1 q_w) & q_w^2 - q_x^2 - q_y^2 + q_z^2 \end{bmatrix} \tag{3.2.8}$$

between the attitude matrix and the related attitude quaternion, the attitude evolution results:

$$\dot{\boldsymbol{q}}_{B/L} = \frac{1}{2}\boldsymbol{\Omega}_{B/L}\boldsymbol{q}_{B/L} \tag{3.2.9}$$

with

$$\boldsymbol{\Omega}_{B/L} = \begin{bmatrix} 0 & \omega_{B/Lz} & -\omega_{B/Ly} & \omega_{B/Lx} \\ -\omega_{B/Lz} & 0 & \omega_{B/Lx} & \omega_{B/Ly} \\ \omega_{B/Ly} & -\omega_{B/Lx} & 0 & \omega_{B/Lz} \\ -\omega_{B/Lx} & -\omega_{B/Ly} & -\omega_{B/Lz} & 0 \end{bmatrix} \tag{3.2.10}$$

3.2.3 Hold point kinematics

As already stated the scenario of this thesis requires bringing the chaser in a preselected hold point fixed with respect to the body frame to enable the chaser to perform the final capture procedure. Since the chaser is supposed to dock with the target, it is needed the dynamical evolution of the hold point with respect to the LVLH frame, so the position and the velocity result from kinematics relations:

$$\begin{cases} \boldsymbol{r}_d = \boldsymbol{R}_{B/L}^T \boldsymbol{r}_d^B \\ \\ \boldsymbol{v}_d = \boldsymbol{R}_{B/L}^T (\boldsymbol{\omega}_{B/L} \wedge \boldsymbol{r}_d^B) \end{cases} \tag{3.2.11}$$

where the position vector of the desired hold point $\boldsymbol{r}_d$ comes from the hold point position vector $\boldsymbol{r}_d^B$ in the body frame mapped into the LVLH frame by means of the attitude matrix $\boldsymbol{R}_{B/L}$, while the desired hold point velocity vector $\boldsymbol{v}_d$ comes from the rigid body motion kinematics [29].

3.3 Safety constraints

Proximity manoeuvres for an unconstrained chaser may lead the spacecraft to crash against the target causing a dangerous collision, especially in the context of synchronisation with an uncooperative tumbling target. So to handle the collisions avoidance it is needed to introduce a safety constraint on the chaser as depicted in Figure 3.2 taken from [18]:

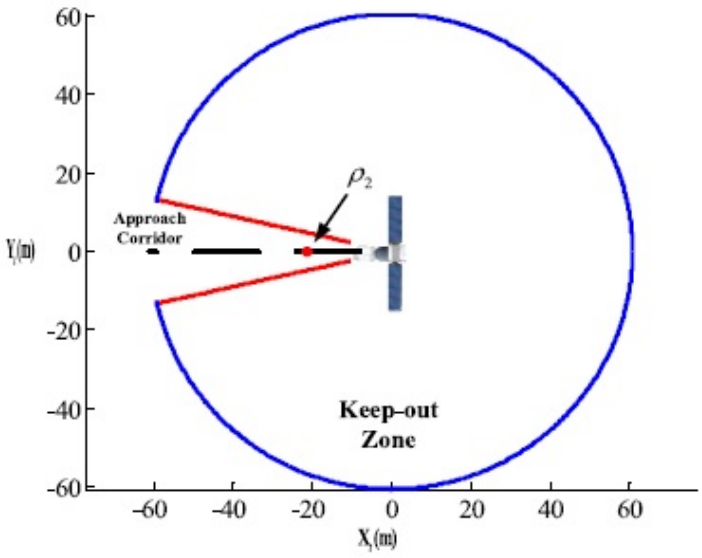

Figura 3.2: Keep in region. Courtesy of: Q.Hu,Y.Liu,Y.Zhang Control of non-cooperative spacecraft in final phase proximity operations under input constraints [18].

Through the literature [8],[21],[13],[27] the types of constraint divide into two main categories:

- Keep out zones, which are safety areas forbidden to the chaser and generally defined by means of simple geometric solids like ellipsoids.
- Approach corridor, typically defined as a cone or a polytope, which constraint the chaser to lay on a restricted region near the target so effectively preventing the collisions.

Benefits of this last kind of constraint come also on the mathematical side: since the conic region defined is convex, if the formulation of the dynamics and the objective are convex too, it is assured the presence of a global minimum in the optimisation process [**90698**]. However, for this thesis investigation since the target involved is tumbling, constraining the trajectory to lie inside a convex region in the case of high target angular regime cause the optimal control to keep the path along some side of the approach corridor. Since the corridor is fixed concerning the body frame and rotating with respect to LVLH one, the spacecraft trajectory ends up in the constraint surface and is subject to its acceleration, so preventing further control cost reduction. Considering instead keep out

zones would in principle enable the chaser to use all the space apart from the forbidden region to exploit the fuel optimisation.

The safety regions depend on the geometrical nature of the target satellite and so to maintain a general perspective these safety regions are considered to be described by 3D conic which in a first approximation, allows to include the main spacecraft geometry plus some simple appendages like solar panels to properly define the surface. Mathematically, a conic is described by a general quadratic form with three kinds of types: elliptic, parabolic and hyperbolic. For this work, only hyperboloid and ellipsoids will be taken into account as is shown in Figure 3.3

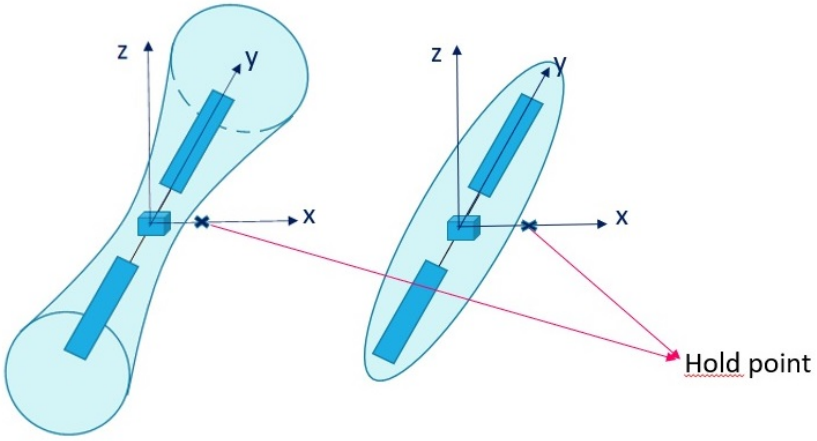

Figura 3.3: Keep out region.

in particular defining the outer region of the conics in the implicit form $S(x, y, z) \geq 0$:

$$\rho(x^2 + z^2 - d^2) - y^2 \geq 0 \tag{3.3.1}$$

$$(\frac{x}{c_x})^2 + (\frac{y}{c_y})^2 + (\frac{z}{c_z})^2 - 1 \geq 0 \tag{3.3.2}$$

where x,y,z are the coordinates of the points belonging to the surfaces, while ρ, d and c_x, c_y, c_z are respectively constant coefficients shaping the the hyperboloid and the ellipsoid. Equations 3.3 and 3.3 can be generally represented as:

$$\boldsymbol{r}^T \boldsymbol{C} \boldsymbol{r} - 1 \geq 0 \tag{3.3.3}$$

where the matrix $\boldsymbol{C}$ is a diagonal matrix containing the conic geometric coefficients.

Capitolo 4

Close approach control strategy

4.1 Optimal control theory

Optimal control theory provides the tools to minimise a certain objective function when a dynamical system is subject to constraints. For trajectories problems the control derived is used to move the system from a set of initials conditions to an ending one, constituting a two-point boundary value problem, minimising fuel cost or energetic criteria.

Two categories of methods are available to solve an optimal control problem: indirect methods and direct ones. In the first, optimal control theory is applied to ensure the minimisation conditions leading to a well-defined boundary value problem. The related numerical solution involve usually single or multiple shooting methods. The other philosophy, the direct methods, requires the discretisation of the equations and the objective minimisation by imposing the dynamics on a collocated trajectory.

However several limitations affect both typologies: although providing high accuracy and low computational cost and time, indirect methods suffer the complexity structure of constraints and the optimality of the solution, which is highly dependent on initial guess [14]. At the contrary direct method easily handle all the nonlinearity of problem formulation but at the price of a higher computational cost, lower accuracy and strong dependence on initial guess [4]. So several simplified methods have been developed trying to tackle the optimal problem but meanwhile obtaining sub-optimal solution as shown in Figure 4.1, taken from [38].

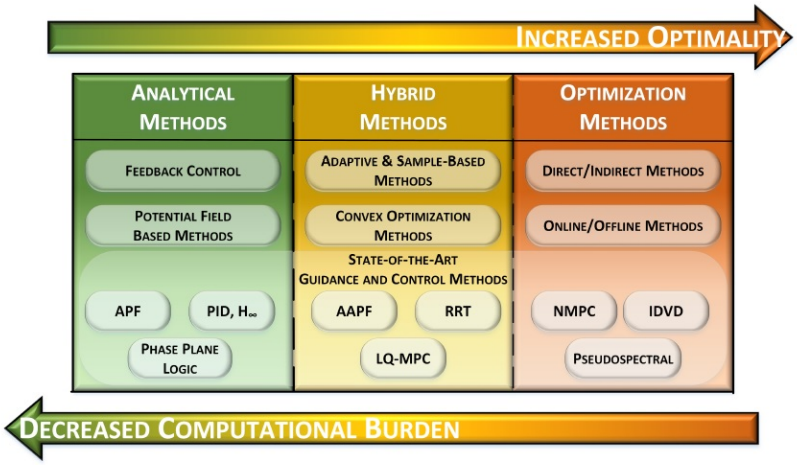

Figura 4.1: Control methods. Courtesy of: R.S. Zappulla, Experimental evaluation methodology for spacecraft proximity maneuvers in adynamic environment [38].

The table summarises the state of the art trade-off between optimality and computational efficiency and analytical handleness.

4.1.1 Full control problem formulation

The problem studied in this work is a time fixed two-point boundary value problem subject to path constraint which allows the chaser to avoid collisions while the propellant reduction is achieved by imposing the minimisation of the classical energetic quadratic cost typical of linear systems:

$$min \quad J = \int_{t_0}^{t_f} \frac{\boldsymbol{u}(t)^T \boldsymbol{u}(t)}{2} \, dt \tag{4.1.1}$$

subject to dynamics:

$$\delta \dot{\boldsymbol{\alpha}}(t) = \boldsymbol{A} \delta \boldsymbol{\alpha}(t) + \boldsymbol{B}(t) \boldsymbol{u}(t) \tag{4.1.2}$$

and with boundary values conditions

$$\begin{cases} \delta \boldsymbol{\alpha}(t_0) = \delta \boldsymbol{\alpha}_0 \\ \delta \boldsymbol{\alpha}(t_f) = \delta \boldsymbol{\alpha}_f \end{cases} \tag{4.1.3}$$

To complete the formulation, the path constraint is introduced. As described in the

last paragraph of the previous chapter keep-out regions to ensure safety collision-free trajectories have been adopted using ellipsoid and hyperboloid surfaces.

Since the formulation is in ROE, it is quite simple to convert the pure cartesian geometric constraint in the new basis by means of Equation 3.1.12 so that it results:

$$\boldsymbol{r}(t) = \boldsymbol{R}(t)\tilde{\boldsymbol{T}}(t)\delta\boldsymbol{a}(t) \tag{4.1.4a}$$

$$\boldsymbol{r}^T\boldsymbol{C}\boldsymbol{r} \geq 1 \tag{4.1.4b}$$

where $\boldsymbol{R}(t)$ is the rotation matrix obtained from the propagation of the target attitude:

$$\begin{cases} \boldsymbol{J}\dot{\boldsymbol{\omega}} + \boldsymbol{\omega} \wedge \boldsymbol{J}\boldsymbol{\omega} = \boldsymbol{T}_{gg} \\ \dot{\boldsymbol{q}}_{B/L} = \frac{1}{2}\boldsymbol{\Omega}_{B/L}\boldsymbol{q}_{B/L} \\ \boldsymbol{R}_{B/L} = \boldsymbol{R}_{B/L}(\boldsymbol{q}_{B/L}) \end{cases} \tag{4.1.5}$$

where the integration is made by means of a fourth order Runge-Kutta method implemented in the ode45™ MATLAB™ function.

4.2 Impulsive control formulation

To overcome the complexity provided by the optimal control formulation it is useful to translate into the domain of nonlinear programming, where a proper discretisation is introduced to suitably integrate the differential equation of dynamics with the prescribed control. Of course here the system being discrete is a finite dimension problem against the original infinite dimension optimal control one, but working out the optimization of the nonlinear problem the resultant solution which is suboptimal concerning the original problem can in principle recover the optimality of the solution increasing the discretisation nodes theoretically through the infinite limit [4].

Among the nonlinear programming formulations for this problem, here impulsive controls are chosen among the admissible function because of the well establish literature background in planning relative trajectories [36], taking advantage of the state transition matrix of the system. Finally despite being a limited assumption for low-thrust systems, it is possible to recover analytically the continuous thrust profile as done in [26].

Given the chaser dynamics as a linear system in the relative ROE state space:

$$\delta\dot{\boldsymbol{\alpha}}(t) = \boldsymbol{A}\delta\boldsymbol{\alpha}(t) + \boldsymbol{B}(t)\boldsymbol{u}(t) \tag{4.2.1}$$

The formal solution is provided by the Lagrange formula [25]:

$$\delta\boldsymbol{\alpha}(t) = e^{\int_{t_0}^{t} \boldsymbol{A}(\tau)\, d\tau}\delta\boldsymbol{\alpha}_0 + \int_{t_0}^{t} e^{\int_{t_0}^{t-\tau} \boldsymbol{A}(s)\, ds}\boldsymbol{B}(\tau)\boldsymbol{u}(\tau)\, d\tau \tag{4.2.2}$$

or more compactly

$$\delta\boldsymbol{\alpha}(t) = \boldsymbol{\Phi}(t, t_0)\delta\boldsymbol{\alpha}_0 + \int_{t_0}^{t} \boldsymbol{\Phi}(t, \tau)\boldsymbol{B}(\tau)\boldsymbol{u}(\tau)\, d\tau \tag{4.2.3}$$

where $\boldsymbol{\Phi}$ is the state transition matrix. Representing the solution of the linear system, the state transition matrix satisfies the following property [25]:

$$\begin{cases} \dot{\boldsymbol{\Phi}}(t, t_0) = \boldsymbol{A}\boldsymbol{\Phi}(t, t_0) \\ \boldsymbol{\Phi}(t_0, t_0) = \boldsymbol{I} \end{cases} \tag{4.2.4}$$

Having chosen impulsive control, the resulting admissible function is the Dirac comb function weighted by the instantenous velocity increment provided by the thrusters at the respective instant of time:

$$\boldsymbol{u}(t) = \sum_{i=1}^{N} \delta(t - t_i)\Delta\boldsymbol{v}_i \tag{4.2.5}$$

where the times t_i are equally spaced from an initial to final time. Fynally substituting back the obtained control into the convolution integral, it results:

$$\delta\boldsymbol{\alpha}(t) = \boldsymbol{\Phi}(t, t_0)\delta\boldsymbol{\alpha}_0 + \sum_{i=1}^{N} \boldsymbol{\Phi}(t, t_i)\boldsymbol{B}(t_i)\Delta\boldsymbol{v}_i \tag{4.2.6}$$

4.2.1 Dynamic and geometric constraints

Since the control problem is a boundary value one, it must be imposed the matching of the endpoint of the trajectory with the position of the hold point at the final time, namely conditions in Equation 4.1.3. Starting from the solution derived in Equation 4.2.6, evaluating the expression at the final time and recasting it into matrix notation, results:

$$\underbrace{\begin{bmatrix}\boldsymbol{\Phi}(t_f,t_1)\boldsymbol{B}(t_1) & \dots & \boldsymbol{B}(t_f)\end{bmatrix}}_{\boldsymbol{A}_{eq}}\underbrace{\begin{bmatrix}\Delta\boldsymbol{v}_1\\ \vdots \\ \Delta\boldsymbol{v}_N\end{bmatrix}}_{\boldsymbol{v}} = \underbrace{\delta\boldsymbol{\alpha}_f - \boldsymbol{\Phi}(t_f,t_0)\delta\boldsymbol{\alpha}_0}_{\boldsymbol{b}_{eq}} \tag{4.2.7}$$

which is a simple linear system of equality constraints

$$\boldsymbol{A}_{eq}\boldsymbol{v} = \boldsymbol{b}_{eq} \tag{4.2.8}$$

The next step involves the process to impose the trajectory to respect the safety keep-out zones defined by 4.1.4. Since the control is impulsive and the state is evaluated at N points, this corresponds to the imposition of N points of the trajectory namely at each $\boldsymbol{r}_k = \boldsymbol{r}(t_k)$. Using Equations 4.2.6 and 4.1.4 results:

$$\boldsymbol{r}(t) = \boldsymbol{R}(t)\boldsymbol{T}(t)\boldsymbol{\Phi}(t,t_0)\delta\boldsymbol{\alpha}_0 + \boldsymbol{R}(t)\boldsymbol{T}(t)\sum_{i=1}^{N}\boldsymbol{\Phi}(t,t_i)\boldsymbol{B}(t_i)\Delta\boldsymbol{v}_i \tag{4.2.9}$$

Evaluating this expression at each N points and arranging into matrices results:

$$\begin{bmatrix}\boldsymbol{r}_1\\ \vdots \\ \boldsymbol{r}_N\end{bmatrix} = \underbrace{\begin{bmatrix}\boldsymbol{R}_1\boldsymbol{T}_1\boldsymbol{\Phi}_{1,1}\boldsymbol{B}_1 & \dots & \boldsymbol{0}_{3x3}\\ \vdots & \ddots & \vdots \\ \boldsymbol{R}_N\boldsymbol{T}_N\boldsymbol{\Phi}_{N,1}\boldsymbol{B}_1 & \dots & \boldsymbol{R}_N\boldsymbol{T}_N\boldsymbol{\Phi}_{N,N}\boldsymbol{B}_N\end{bmatrix}}_{\boldsymbol{A}_l}\underbrace{\begin{bmatrix}\Delta\boldsymbol{v}_1\\ \vdots \\ \Delta\boldsymbol{v}_N\end{bmatrix}}_{\boldsymbol{v}} + \underbrace{\begin{bmatrix}\boldsymbol{R}_1\boldsymbol{T}_1\boldsymbol{\Phi}_{1,1}\delta a_0\\ \vdots \\ \boldsymbol{R}_N\boldsymbol{T}_N\boldsymbol{\Phi}_{N,1}\delta a_0\end{bmatrix}}_{\boldsymbol{b}_l} \tag{4.2.10}$$

In order to impose the k^{th} position constraints:

$$\boldsymbol{r}_k^T\boldsymbol{C}\boldsymbol{r}_k \geq 1 \tag{4.2.11}$$

a block diagonal servicing matrix is introduced to encode the geometric properties of the selected keep-out zones:

$$\boldsymbol{C}^k = \begin{bmatrix} \ddots & & \\ & \boldsymbol{C} & \\ & & \ddots \end{bmatrix} \tag{4.2.12}$$

and substituting the value of 4.2.10 into 4.2.1, finally results:

$$\boldsymbol{v}^T \underbrace{\boldsymbol{A}_l^T \boldsymbol{C}^k \boldsymbol{A}_l}_{A_{ineq}^k} \boldsymbol{v} + \boldsymbol{v}^T \underbrace{2\boldsymbol{A}_l^T \boldsymbol{C}^k \boldsymbol{b}_l}_{\boldsymbol{b}_{ineq}^k} + \underbrace{\boldsymbol{b}_l^T \boldsymbol{C}^k \boldsymbol{b}_l - 1}_{c_{ineq}^k} \geq 0 \tag{4.2.13}$$

which are the conics constraints but now in the control space for each impulse $k = 1 \dots N$.

4.3 Optimisation problem

4.3.1 Quadratic constrained Quadratic Programming

Finally, the optimal control problem assumes the form of a quadratic constrained quadratic programming [3]:

$$\min J = \frac{1}{2} \boldsymbol{v}^T \boldsymbol{v} \tag{4.3.1}$$

subject to:

$$\begin{cases} \boldsymbol{A}_{eq} \boldsymbol{v} = \boldsymbol{b}_{eq} \\ \boldsymbol{v}^T \boldsymbol{A}_{ineq}^k \boldsymbol{v} + \boldsymbol{v}^T \boldsymbol{b}_{ineq}^k + c_{ineq}^k \geq 0 \qquad k = 1 \dots N \\ -\boldsymbol{v}_{max} \leq \boldsymbol{v} \leq \boldsymbol{v}_{max} \end{cases} \tag{4.3.2}$$

This class of problem lies in the domain of nonlinear programming, reducing to the convex case only in the presence of the negative definiteness of the $\boldsymbol{A}_{ineq}^k$ matrices of the quadratic inequality constraints in 4.3.2. For general non-convex QCQPs, the prevailing method to tackle the problem is through semidefinite relaxation [22], however for this work it has been

decided to face the full problem using MATLAB™ built-in function fmincon™, selecting the interior point algorithm option and providing the espression of the graient and of the hessian of the problem since the derivatives involved are simply the matrices present in the quadrics. Dealing with a nonconvex problem, the solution is not guaranteed to be unique so it is convenient from a numerical point of view to start with a good guess, avoiding as much as possible to end in local minima. Therefore, it is useful to consider first the suboptimal solution of the unconstrained problem as an initial guess:

$$\min J = \frac{1}{2}\boldsymbol{v}_{guess}^T \boldsymbol{v}_{guess} \tag{4.3.3}$$

subject to:

$$\begin{cases} \boldsymbol{A}_{eq}\boldsymbol{v}_{guess} = \boldsymbol{b}_{eq} \\ \\ -\boldsymbol{v}_{max} \leq \boldsymbol{v}_{guess} \leq \boldsymbol{v}_{max} \end{cases} \tag{4.3.4}$$

which is a standard convex quadratic programming. In order to speed up the solution process as much as possible, a further simplification is considered removing from 4.3.4 the upper and lower velocity limit, obtaining an optimisation problem that admits a straightforward solution [3]

$$J = \frac{1}{2}\boldsymbol{v}_{guess}^T \boldsymbol{v}_{guess} - \boldsymbol{\lambda}^T(\boldsymbol{A}_{eq}\boldsymbol{v}_{guess} - \boldsymbol{b}_{eq}) \tag{4.3.5}$$

where the equality constraint has been adjoined to the functional by means of the Lagrange multiplier vector λ. Following classical minimisation by imposing the functional gradient to be zero, the problem reduces to a simple linear system:

$$\begin{bmatrix} \boldsymbol{I} & -\boldsymbol{A}_{eq}^T \\ \boldsymbol{A}_{eq} & \boldsymbol{O} \end{bmatrix} \begin{bmatrix} \boldsymbol{v}_{guess} \\ \boldsymbol{\lambda} \end{bmatrix} = \begin{bmatrix} \boldsymbol{o} \\ \boldsymbol{b}_{eq} \end{bmatrix} \tag{4.3.6}$$

whose analytical solution is:

$$\boldsymbol{v}_{guess} = \boldsymbol{A}_{eq}^T(\boldsymbol{A}_{eq}\boldsymbol{A}_{eq}^T)^{-1}\boldsymbol{b}_{eq} \tag{4.3.7}$$

Capitolo 5

Simulations and results

5.1 Case study definition

In order to test the control strategy described in the previous section to obtain an optimal guidance reference trajectory, two distinct scenarios are considered based on the topology of the keep-out regions namely ellipsoid and hyperboloid. The second case although being much more conservative and restrictive is useful to avoid dangerous target areas with large appendages while in close proximity.

In Table 5.1 are reported respectively the main parameters driving the attitude dynamics of the Envisat [5]:

Target initials conditions	$\boldsymbol{\omega}$ [°/s]	**Precession** $\boldsymbol{\alpha}$ [°]	**Attitude** $\boldsymbol{q_{error}}$	**Inertia** **J** [kg$\boldsymbol{m^2}$]
	5	1.7	[0;0;0;1]	Jx = 127000 , Jy = 17000 , Jz = 127000

Tabella 5.1: Target initial conditions.

Among the others are specified the angular rate magnitude and the inclination α of the target angular velocity with respect to the Z-axis, in the body frame, which gives rise to a precession. The attitude error is defined between the body frame and the LVLH one, and with the initial value set to have the body main axis aligned with the LVLH frame. Finally are reported the target inertia assuming and axisymmetric inertia matrix [10].

In table 5.2 are reported the target keep-out region geometric parameters:

Keep-out region	**Cx [m]**	**Cy [m]**	**Cz [m]**	**Cone aperture ρ**	**d [m]**	**Hold point X-axis [m]**
	8	16	8	$\tan(15°)$	8	10

Tabella 5.2: Target keep-out region geometry.

The hold point position is fixed along the X-axis of the body frame. The C coefficients are the shaping constants of the ellipsoid as was defined in Equation 3.3 and reported here for clarity:

$$(\frac{x}{c_x})^2 + (\frac{y}{c_y})^2 + (\frac{z}{c_z})^2 - 1 \geq 0 \tag{5.1.1}$$

The hyperboloid keep-out region is instead defined using the radius d and an aperture cone ρ, again related to Equation 3.3:

$$\rho(x^2 + z^2 - d^2) - y^2 \geq 0 \tag{5.1.2}$$

Before showing the results obtained testing multiple approach initial conditions scenario, here are introduced a set of initial conditions for the chaser in table 5.3, which are used in the next two subsections to show the behaviour of the algorithm respectively in the case of ellipsoid and hyberboloid. The tables provide also the orbital altitude of the target and its orbital angular velocity n here considered constant in the hypothesis of near circular orbit. Concerning instead the velocity vector of the chaser, it is supposed an energy matching condition coherent with the setting of the preliminary inspection phase.

Chaser initials	**Altitude [km]**	**n [1/s]**	**Position r [m]**	**Velocity v [m/s]**
	800	0.001	[50;0;0]	[0;-0.1040;0]

Tabella 5.3: Chaser initial conditions.

In the following section are presented the validation simulations for two scenarios:

- CASE A: elliptic keep out region.

- CASE B: hyperbolic keep out region.

The time duration is imposed to 72 s, which is the target angular rotation period, and the control is subject to a limitation for each single velocity impulses of 0.5 m/s.

5.1.1 Case A

In this section are presented the results for case A where in figure 5.1 is shown the trajectory viewed respectively in the LVLH frame and in the body frame, with the target fully enclosed in a general ellipsoid as plotted in the figure.

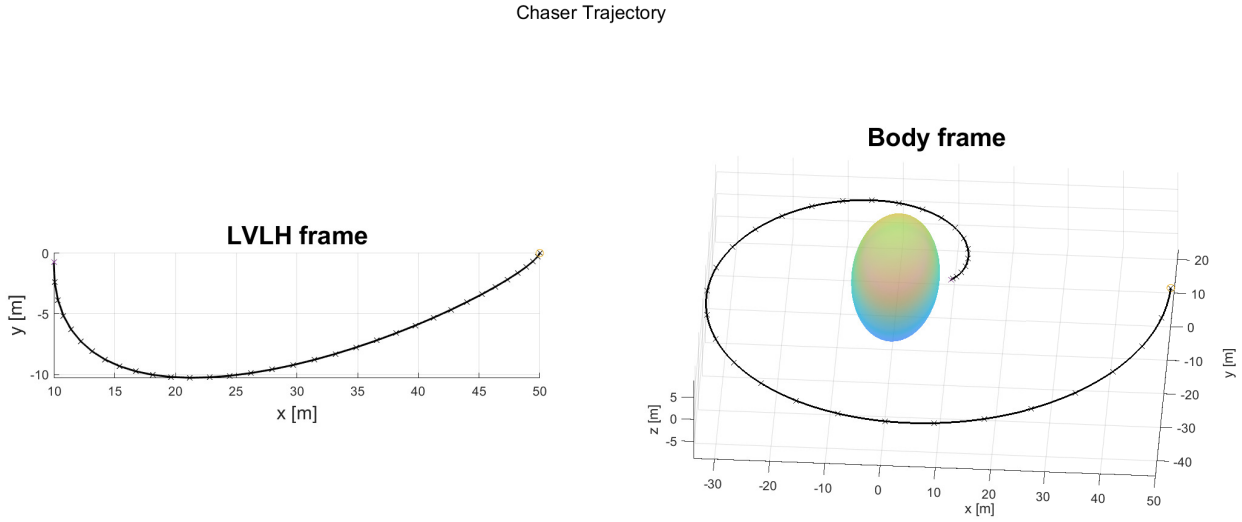

Figura 5.1: Chaser trajectory.

In Figure 5.2 the position and velocity error with respect to the final condition and with the velocity plot on the right showing discontinuities due to the applied impulses are shown respectively.

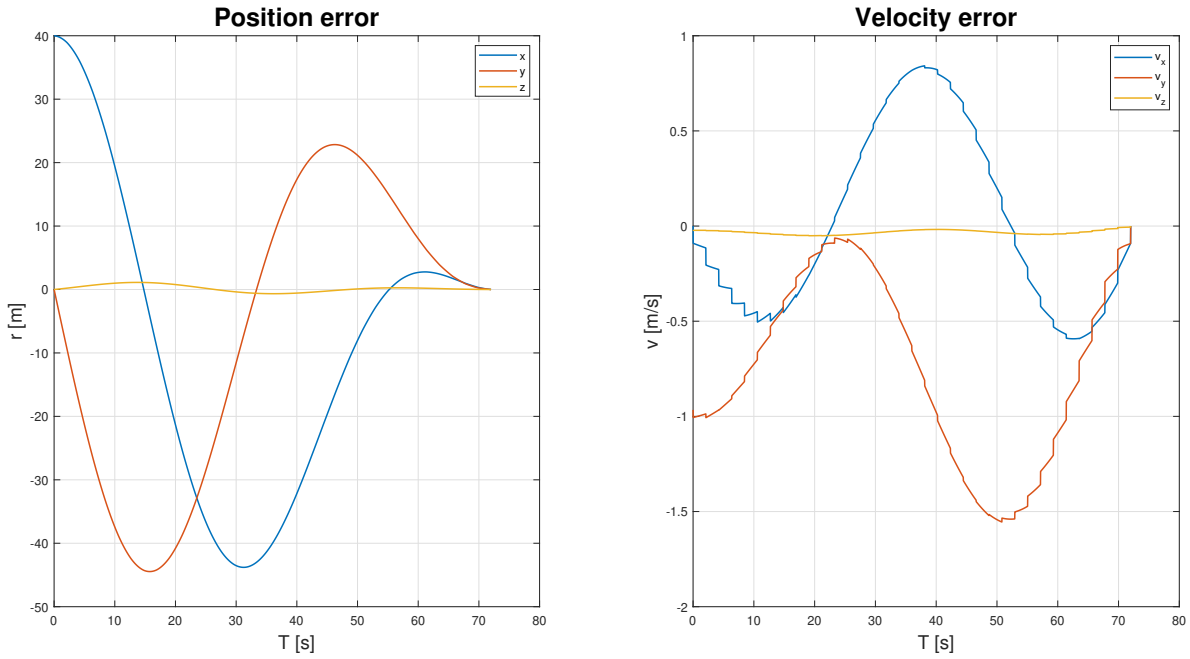

Figura 5.2: Position and Velocity error.

The sinusoidal behaviour of both the errors plots is closely related to the near-circular motion of the hold point with respect to the LVLH frame.

Finally, in figure 5.3 the control impulses components and their associated magnitudes are reported.

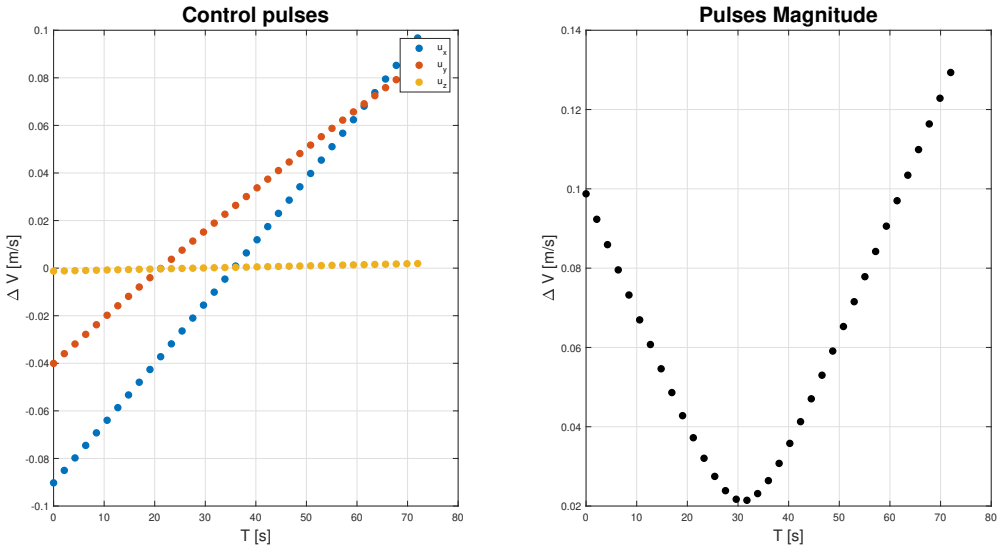

Figura 5.3: Control Pulses.

As can be noticed, to perform the spiralling synchronisation plotted in Figure 5.1, the guidance system introduces impulses of decreasing-increasing magnitude to assure the required position and velocity alignment.

The total ΔV cost required for this manoeuvre is equal to 2.2522 m/s.

5.1.2 Case B

The aim of is section is identical to the previous and provides the guidance trajectory starting from the same initial condition but this time subject to the hyperbolic keep-out region which modifies the behaviour of the trajectory as shown in Figure 5.4.

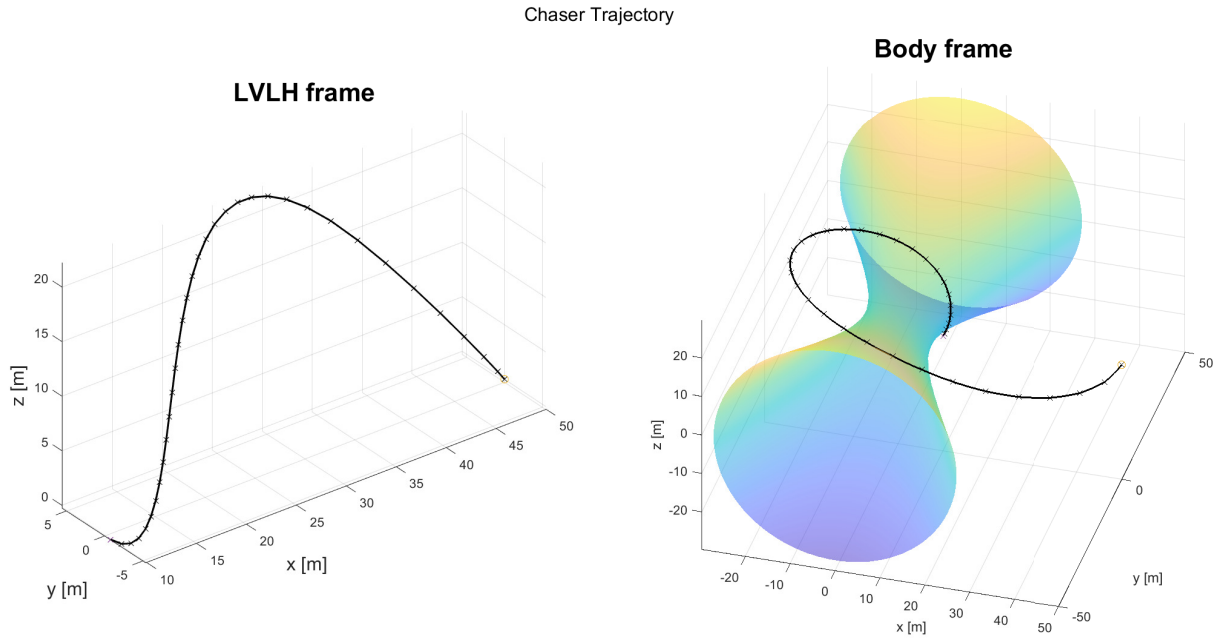

Figura 5.4: Chaser trajectory.

With respect to case A here the chaser has to cope with the topology of the hyperboloid keep-out zone and the guidance scheme introduce an out of plane motion to avoid the safety region which can be seen clearly in Figure 5.5.

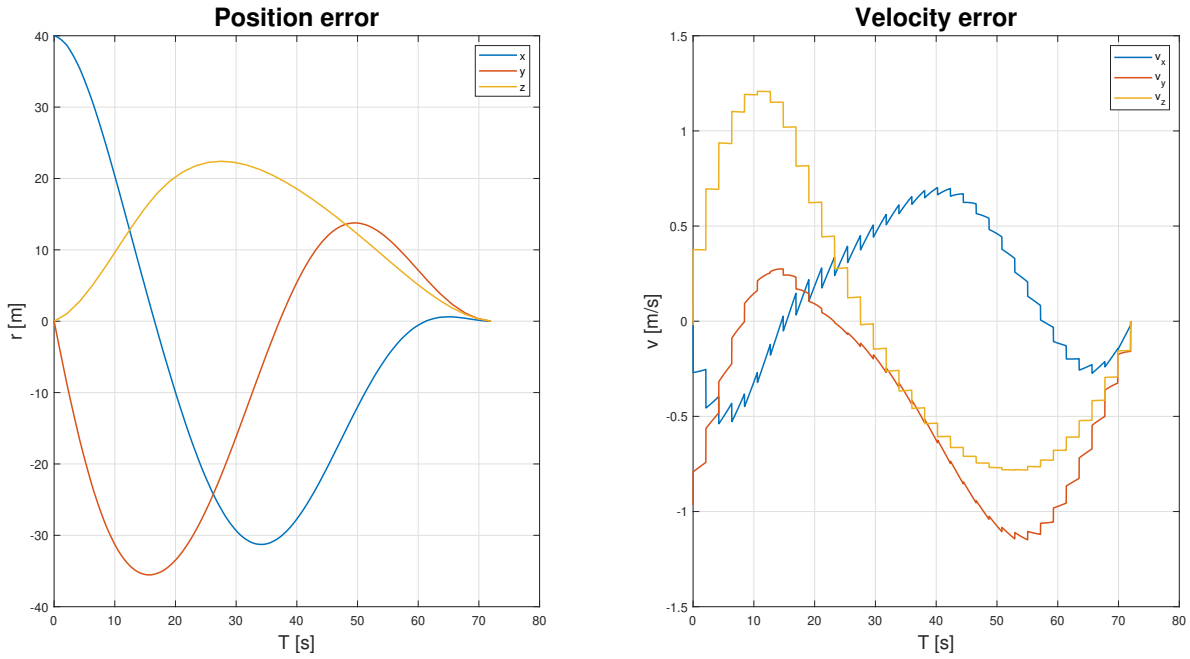

Figura 5.5: Position and velocity error.

Finally observing Figure 5.6 now the trend of the impulses is no more monotonic as in case A, but each components present two legs, one decreasing while the other is increasing in order to makes the spiral synchronisation to cope with the presence of the hyperboloid constraint to avoid collision.

Finally observing Figure 5.6 now the trend of the impulses is no more monotonic as in case A, with the behaviour of the x component of the control opposed to the others directions. Together with the impulse necessary for a spiral synchronisation, here also an out-of-plane component is introduced to cope with the presence of the hyperboloid constraint to avoid collisions.

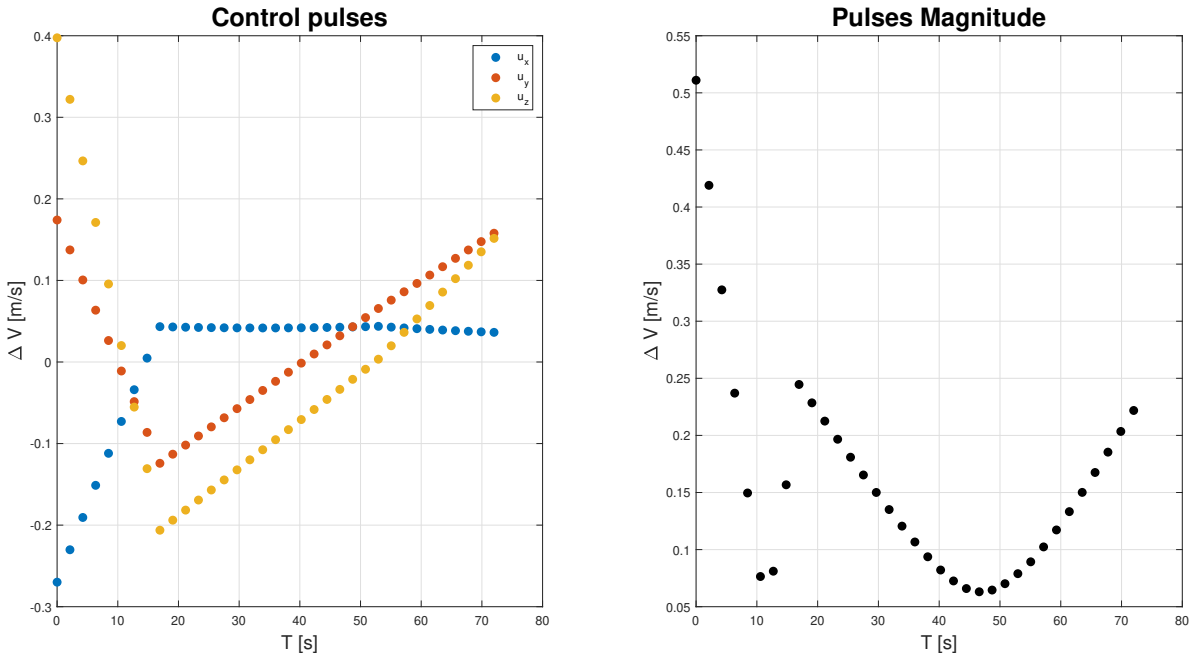

Figura 5.6: Control pulses.

The required ΔV cost is 5.6606 m/s, which is more than double respect to the 2.2522 m/s needed for case A, and the reason stems from the induced out of plane motion.

5.1.3 Scenarios of the cases

Before moving to full testing of the guidance algorithm, the results associated with various possible attitude scenarios are presented in this section. In particular, are considered the effects on the chaser trajectory when the main component of the target angular rate is directed respectively on the x or y or z body axis. The trajectories are plotted in Figure 5.7.

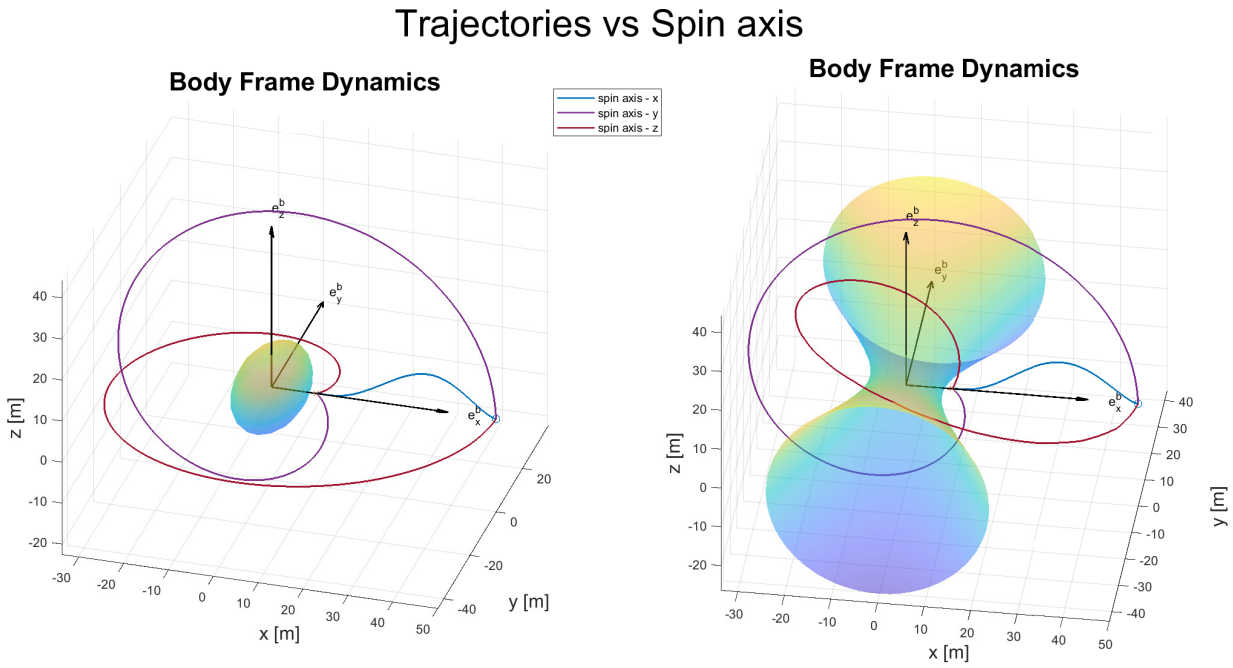

Figura 5.7: Angular regime vs trajectory.

It follows that for both cases starting from the same initial condition the most demanding trajectory in terms of safety is related to the scenario with the spin axis aligned with z axis direction and orthogonal to the plane containing the hold point, since for the other trajectory the safety constraint appears to be inactive making the guidance easier to handle.

5.2 Monte Carlo analysis

In this chapter, the framework to validate the control system proposed in the previous chapter by means of a Monte Carlo method is set up. The interesting property to evaluate is the propellant mass cost in terms of ΔV required to synchronise the chaser with the hold point. The main parameters affecting the problems are the time of duration of the manoeuvre, the number of impulses, the relative initials position and velocity, the angular regime of the chaser.

5.2.1 Final time and discretisation definition

In order to save computational time and resource a reparametrisation of the involved parameters is performed as follows:

$$t_f = k\frac{2\pi}{\omega_0} \tag{5.2.1}$$

for the final time where now the new parameters are the nominal target angular velocity ω_0 and the multiple integer or semi-integer k of the target rotating period.

Instead for the selection of the number of nodes is employed an empiric criteria. Starting from a qualitative analysis, in order to assure that all trajectory satisfies the safety constraint, it results that number of nodes increase due to two parameters, the multiple number k and the angular rate giving:

- low k low $\omega_0 \Rightarrow$ low N
- low k high $\omega_0 \Rightarrow$ medium N
- high k low $\omega_0 \Rightarrow$ medium N
- high k high $\omega_0 \Rightarrow$ high N

From this is natural to consider in a first approximation a linear dependence as

$$N = \lceil \alpha k + \beta \omega \rceil \tag{5.2.2}$$

where two parameters with $\alpha = 10$ and $\beta = 3$ are the first integers numbers that allow for a feasible solution satisfying the safety constraints for both the keep-out zones types.

5.2.2 Spatial initial conditions

The initial conditions for the control problems are rewritten as a function of polar coordinates while the velocities are constrained to be a function of the positions imposing the initial orbit to be in energy matching and centred with respect to the target:

$$\begin{cases} x_0 = r\cos\theta\cos\phi \\ y_0 = r\sin\phi \\ z_0 = r\sin\theta\cos\phi \end{cases} \tag{5.2.3}$$

$$\begin{cases} v_{x0} = \frac{n}{2}y_0 \\ v_{y0} = -2nx_0 \\ v_{z0} = 0 \end{cases} \tag{5.2.4}$$

Given the initial cartesian state the ROE one is obtained with the inverse of the map introduce in 3.1.12 and valued at t_0.

5.2.3 Results case A

Time dependence

Since the guidance formulation is based on a fixed time like optimal control it is interesting to study the cost as a function of final time. So first considering the chaser to be in front of the hold point at an initial position of 50 m, several simulations varying the final time are performed and the result is shown in figure 5.8. The final time in the plot is expressed as a function of the multiple k, previously defined, of the target rotational period, varying in interval between 72 s and 720 s.

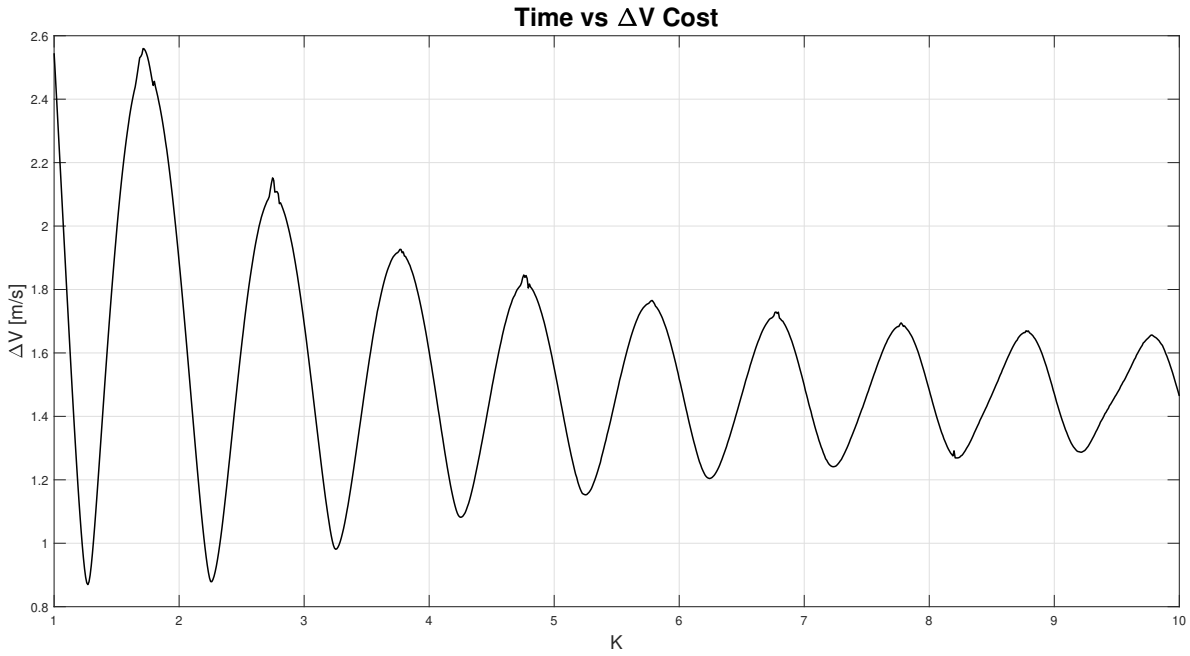

Figura 5.8: Final time associated cost.

Here the decaying oscillator behaviour is due to the following reason: since the keep-out region is limited to the ellipsoid around the origin, most of the trajectory is not subject to geometric constraint and follow the dynamics of the homogeneous CW model; being the harmonic of the CW dynamics much slower than that of the target attitude it results that lower velocity correction is required to change the orbit of the chaser as the final time approach that of target orbit.

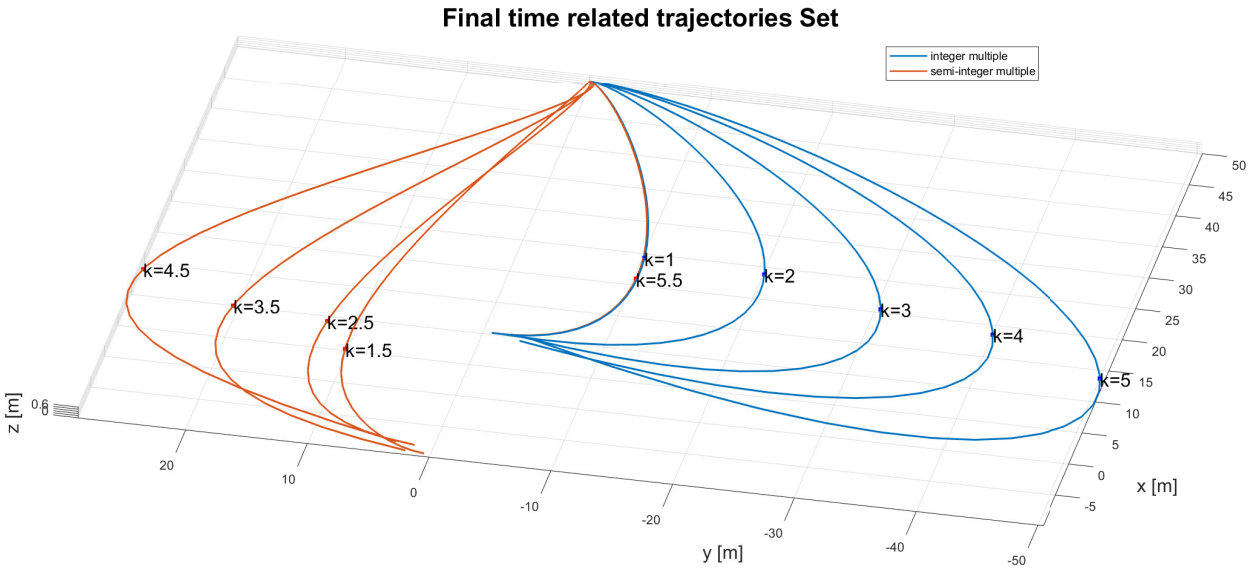

Figura 5.9: Time related trajectories set.

Figure 5.9 provides a spatial visualization in the LVLH frame of the manifold related to the final time, focusing on the trajectory with an integer and semi-integer respectively multiple of time. Since the final time is related to the rotational period around the spin axis nearly orthogonal to the x-y plane, the manifold rightly divide into two family ending in a final position opposite to the other.

Spatial initial condition dependence

In this subsection are presented the Monte Carlo results associated this time to the spatial variation of the initial condition keeping the final time fixed to one target rotational period. Part of the trajectories constituting the manifold associated to the configurational sphere is shown in Figure 5.10.

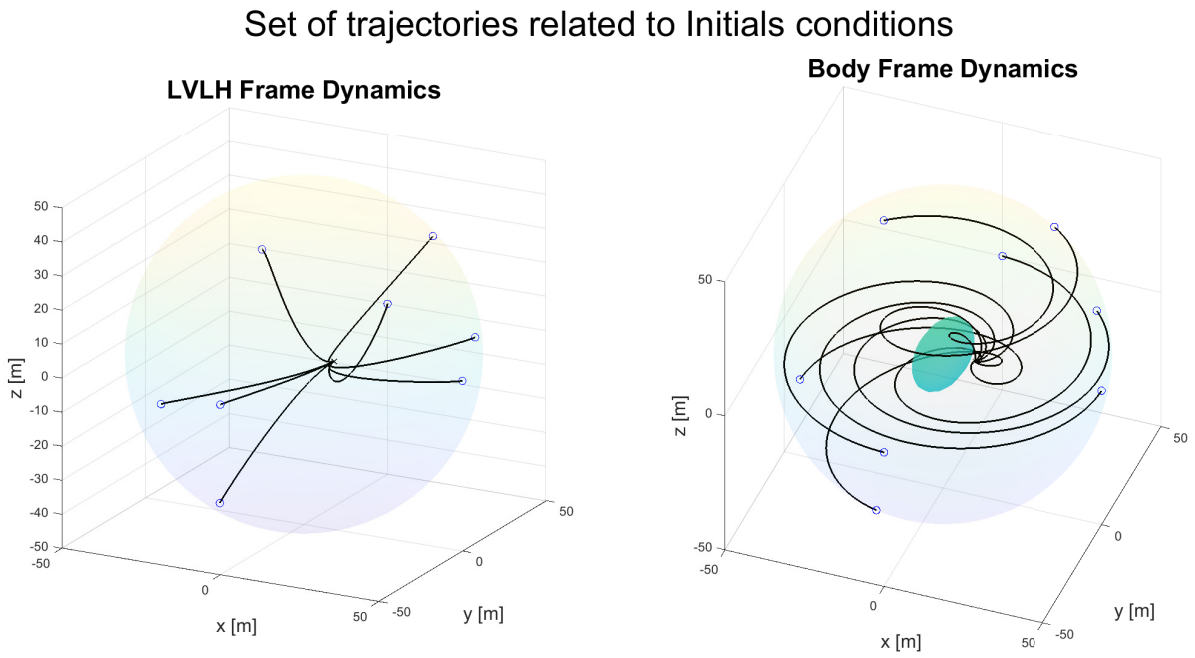

Figura 5.10: Space related trajectories set.

The positions are parametrised with the longitude angle θ and latitude anlge ϕ as given by equation 5.2.3. The variation of the longitude angle induces an out of plane motion clearly seen in the body frame plot of figure 5.10. Although the trajectories share an almost equal spiral-like behaviour, there is a difference in the ΔV cost. Figure 5.11 shows the impulsive control cost related to the angular parameters variation in the initials conditions.

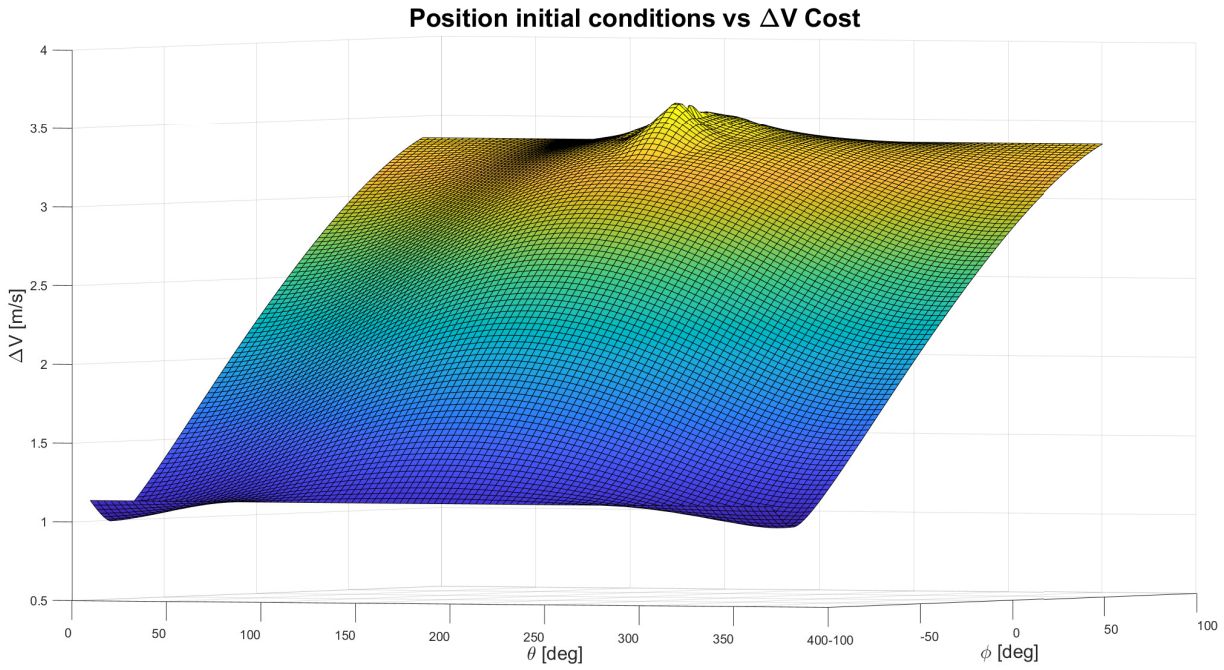

Figura 5.11: Initials condition associated cost.

As can be noticed from the surface plot 5.11, it is evident that the main parameter driving the cost is the latitude angle and this is related to the fact that being the rotation axis mainly orthogonal to the LVLH in-plane trajectory, it follows that for the same longitude angle the variation in latitude affects the safety distance from the ellipsoid.

Spatial and time condition dependence

Finally, for the elliptic case A, Figure 5.12 provides the contour plots of the ΔV cost, in which are considered the results of the mixed effect of the variations in the final time and initial conditions.

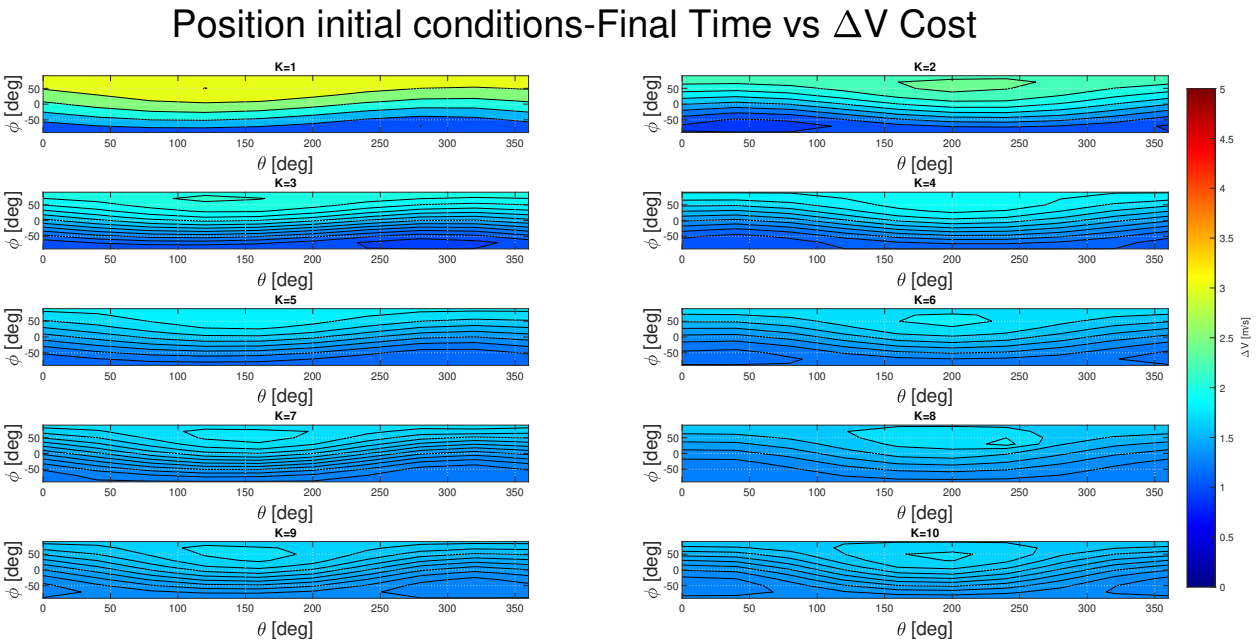

Figura 5.12: Coupled time and space conditions cost.

Considering the entire possible initial position set configuration, the effect of increasing the final time has a different effect on the maxima and minima: the contour line around the minima begins to be deformed from the initial near straight behaviour due to the appearance of two local maxima in the lower extrema of each subplots. Moreover, the peak region tends to enlarge while lowering the maximum value.

5.2.4 Results case B

Time dependence

As done for case A here the same type of analysis is conducted varying the time and keeping the same initial condition presented in 5.1. The computed cost is shown in figure 5.13.

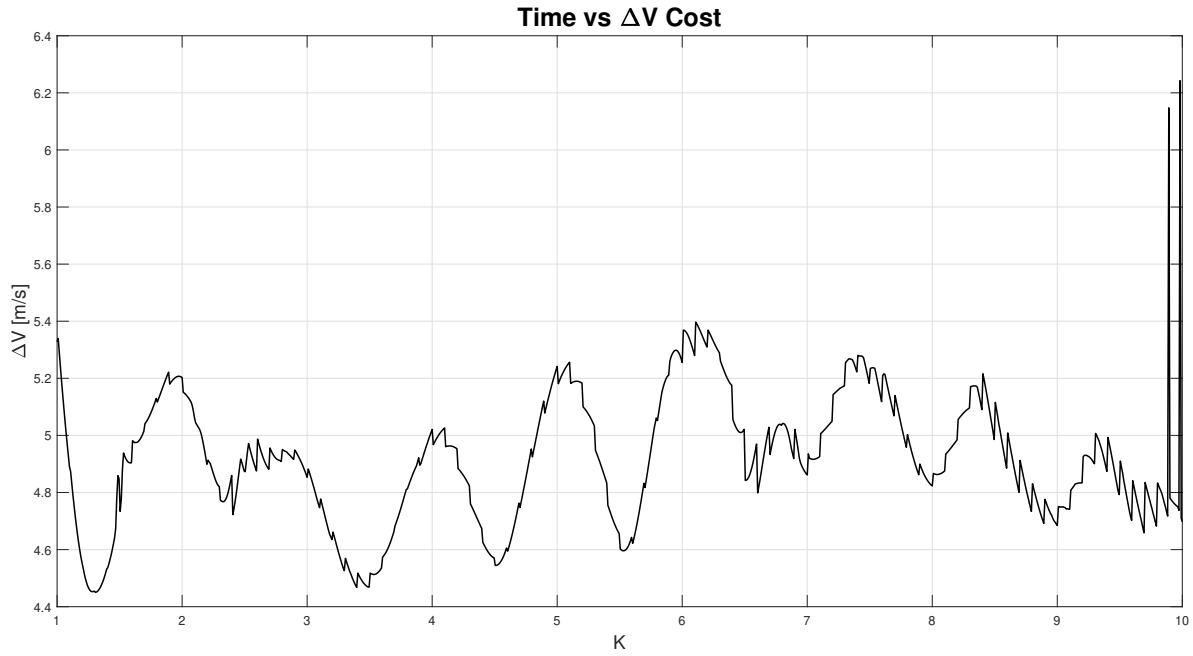

Figura 5.13: Final time associated cost.

This time the behaviour presents a non-smooth oscillation which exchanges the local minima and maxima between integer and semi-integer multiple of the target rotational period, so resulting very different with respect to the case A where the function was smoothly decaying. In fact here the topology of the hyperboloid keep-out zones plays a fundamental role as provides by figure 5.14.

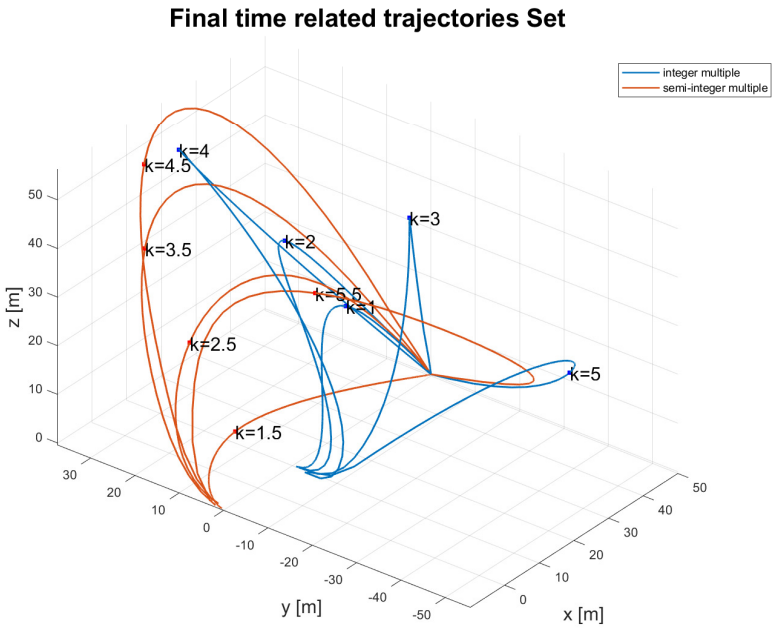

Figura 5.14: Time related trajectories set.

Again the spatial visualization of the manifold is related to several final times, but here the out of plane motion is more pronounced with respect to case A.

Spatial initial condition dependence

In this section are presented the results related to the simulation involving the space condition variation for case B. As done previously the manifold with some trajectories are shown in the LVLH and target body frames are depicted in 5.15.

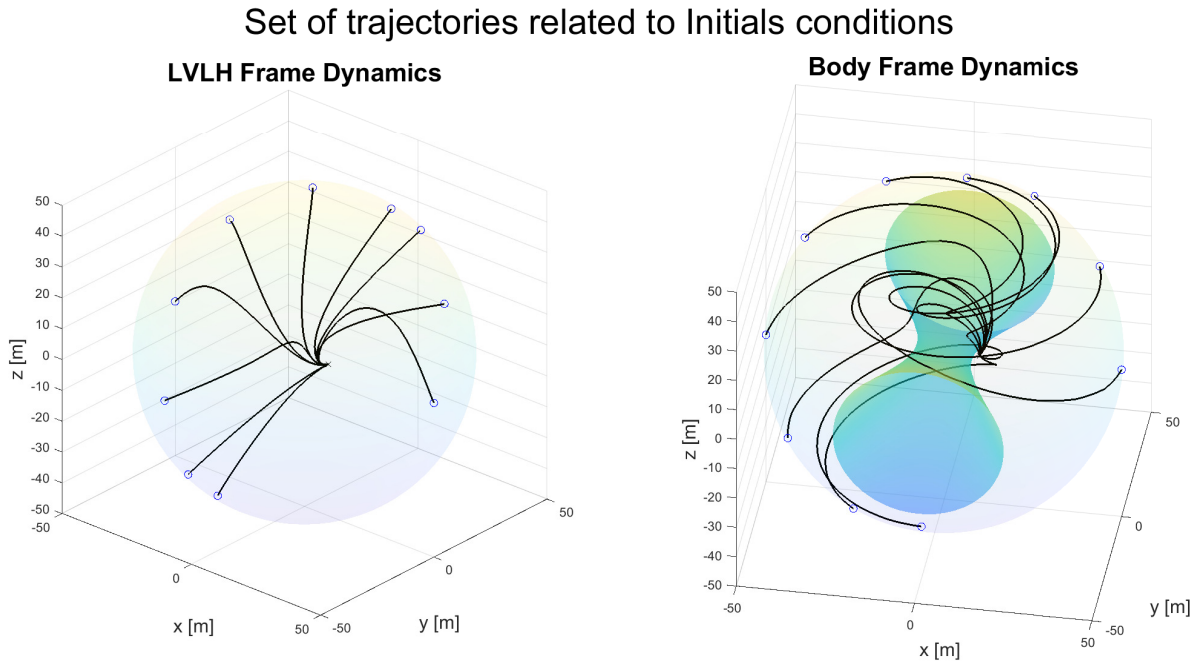

Figura 5.15: Space related trajectories set.

The paths followed by the chaser result to be not as regular as in figure 5.10 due to the surface constraint topology and making the trajectory wrap around the hyperboloid and making so the safety requirements satisfaction much more severe with respect to case A. The related ΔV cost is shown in 5.16.

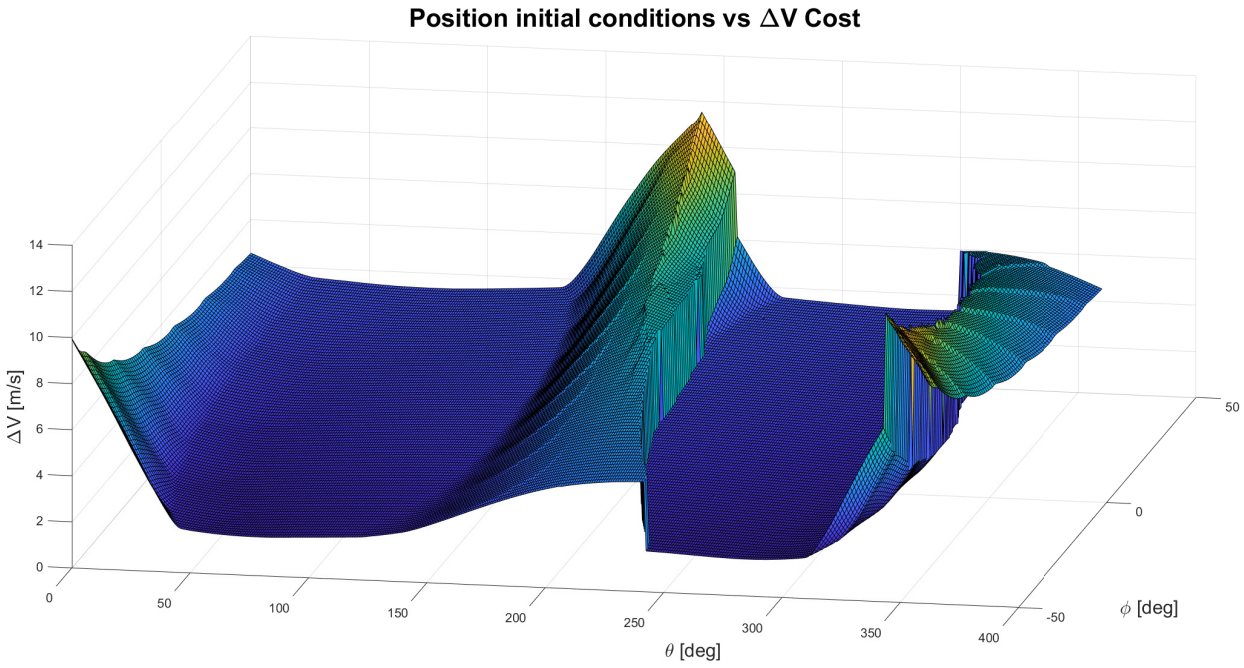

Figura 5.16: Initials condition associated cost.

The surface presents a net separation between the region of minimum energy with the peaks line presenting a discontinuity in the required velocity value. The reason once again lies in the topology: much higher initial impulses are needed for those trajectories starting near above the hold point plane because, for a safe synchronisation, it has to be allowed the safe wrapping around the constrained region.

Spatial and time condition dependence

In the final subsection of this chapter are resumed the cost value for mixed space and time condition. The results obtained are shown in figure 5.17.

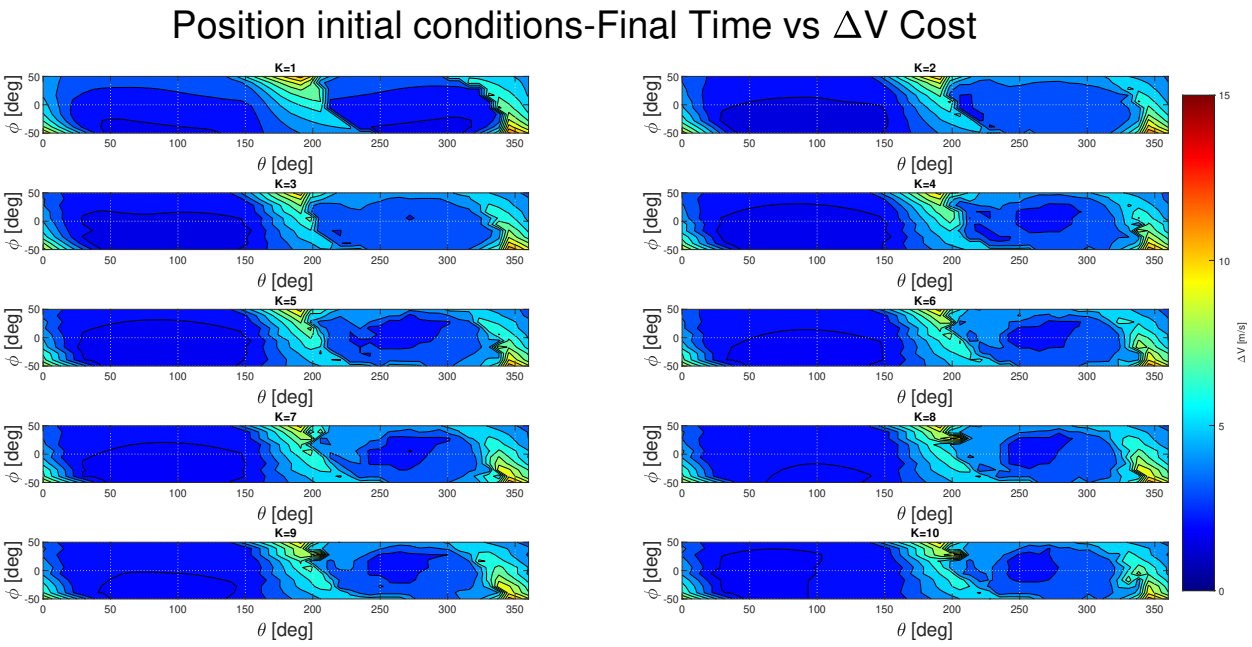

Figura 5.17: Coupled time and space conditions cost.

With respect to case A where new maxima were rising, here the time increase produces the reduction of the hill of maxima, but without max value decrease, and the enlargement of the minima zones towards the right of the plots. The reason stems from the fact that for values of longitude near the hold point plane, the cost to jump over the nearest hyperboloid cone by means of out of plane motion, lowers with time because it is easier to avoid the constrained surface.

Capitolo 6

Conclusion

This work explored the design of an optimal guidance strategy for approaching a tumbling object considering trajectory safety. The safety was enforced considering different conics keep-out-zones around the target, namely elliptical and hyperbolic surfaces. The problem was solved by describing the dynamics in an impulsive fashion, reducing the system to a quadratically constrained quadratic programming problem. To test the proposed guidance algorithm several preliminary case studies were presented to validate the implemented guidance strategy. Then a Monte Carlo analysis was performed to explore the dependence of the initial position conditions of the chaser orbit and the manoeuvre time over the required ΔV consumption necessary to assure a safe synchronisation with the prescribed hold point.

The outcome of the analysis showed that for constant initials positions, the control cost presents a decreasing tendency as the time duration of the manoeuvre is increased for the ellipsoid case, while for the other the cost is subject to oscillation due to the different nature of the safety constraint. Concerning the initial space conditions dependence, the elliptic case showed a lower cost associated with negative latitude values with respect to the symmetry axis of the target, meanwhile being independent of the longitude values due to the symmetric nature of the constraint. Instead, for the hyperbolic case, the minimising longitude values were found to be associated with the out-of-plane position due to the easiness to avoid a collision.

Future possible extension include an analytical reformulation of the optimisation pro-

blem including the number of nodes of time discretisation or deriving a near optimal limiting bound or including them into the variables set. In the latter case the problem becomes mathematically more complex, shifting the QCQP into the domain of integer nonlinear programming and making the numerical computation much more involved. To mitigate this issue a second-order cone programming relaxation might be taken into consideration for the safety constraints, also in the optics to a suitable nonlinear formulation for an onboard MPC implementation.

Bibliografia

[1] Iñigo Alforja Ruiz. "Guidance, Navigation and Control System Design of Envisat Active Debris Removal". In: *repository.tudelft* (2020).

[2] Kyle T Alfriend et al. *Spacecraft formation flying: Dynamics, control and navigation*. Vol. 2. Elsevier, 2009.

[3] Andreas Antoniou e Wu-Sheng Lu. *Practical optimization*. Springer, 2007.

[4] John T Betts. "Survey of numerical methods for trajectory optimization". In: *Journal of guidance, control, and dynamics* 21.2 (1998), pp. 193–207.

[5] Mihir Bhagat. "Convex Guidance for Envisat Rendezvous". In: *Researchgate* (2016).

[6] Nicoletta Bloise et al. "Obstacle avoidance with potential field applied to a rendezvous maneuver". In: *Applied Sciences* 7.10 (2017), p. 1042.

[7] Christophe Bonnal, Jean-Marc Ruault e Marie-Christine Desjean. "Active debris removal: Recent progress and current trends". In: *Acta Astronautica* 85 (2013), pp. 51–60.

[8] George Boyarko, Oleg Yakimenko e Marcello Romano. "Optimal rendezvous trajectories of a controlled spacecraft and a tumbling object". In: *Journal of Guidance, Control, and dynamics* 34.4 (2011), pp. 1239–1252.

[9] Louis Breger e Jonathan P How. "Safe trajectories for autonomous rendezvous of spacecraft". In: *Journal of Guidance, Control, and Dynamics* 31.5 (2008), pp. 1478–1489.

[10] Albert Caubet e James D Biggs. "An inverse dynamics approach to the guidance of spacecraft in close proximity of tumbling debris". In: *researchgate* 7 (2015), p. 9.

[11] CelesTrak. URL: https://www.celestrak.com.

[12] Michelle Chernick e Simone D'Amico. "New closed-form solutions for optimal impulsive control of spacecraft relative motion". In: *Journal of Guidance, Control, and Dynamics* 41.2 (2018), pp. 301–319.

[13] Xiaoyu Chu et al. "Optimised collision avoidance for an ultra-close rendezvous with a failed satellite based on the Gauss pseudospectral method". In: *Acta Astronautica* 128 (2016), pp. 363–376.

[14] Guido Colasurdo e Lorenzo Casalino. "Indirect methods for the optimization of spacecraft trajectories". In: *Modeling and Optimization in Space Engineering*. Springer, 2012, pp. 141–158.

[15] Simone D'Amico. "Autonomous formation flying in low earth orbit". Tesi di dott. TU Delft, 2010.

[16] Stéphane Estable et al. "Capturing and deorbiting Envisat with an Airbus Spacetug. Results from the ESA e. Deorbit consolidation phase study". In: *Journal of Space Safety Engineering* 7.1 (2020), pp. 52–66.

[17] Gabriella Gaias e Marco Lovera. "Safe Trajectory Design For Close Proximity Operations". In: *2020 AAS/AIAA Astrodynamics Specialist Conference*. 2020, pp. 1–15.

[18] Qinglei Hu, Yueyang Liu e Youmin Zhang. "Control of non-cooperative spacecraft in final phase proximity operations under input constraints". In: *Control Engineering Practice* 87 (2019), pp. 83–96.

[19] Qinglei Hu, Jingjie Xie e Chenliang Wang. "Dynamic path planning and trajectory tracking using MPC for satellite with collision avoidance". In: *ISA transactions* 84 (2019), pp. 128–141.

[20] Yoshihiro Ichimura e Akira Ichikawa. "Optimal impulsive relative orbit transfer along a circular orbit". In: *Journal of guidance, control, and dynamics* 31.4 (2008), pp. 1014–1027.

[21] Christopher Michael Jewison. “Guidance and control for multi-stage rendezvous and docking operations in the presence of uncertainty”. Tesi di dott. Massachusetts Institute of Technology, 2017.

[22] Sunyoung Kim e Masakazu Kojima. “Exact solutions of some nonconvex quadratic optimization problems via SDP and SOCP relaxations”. In: *Computational optimization and applications* 26.2 (2003), pp. 143–154.

[23] H Klinkrad. “DISCOS-ESA’s database and information system characterising objects in space”. In: *Advances in Space Research* 11.12 (1991), pp. 43–52.

[24] Adam W Koenig, Tommaso Guffanti e Simone D’Amico. “New state transition matrices for spacecraft relative motion in perturbed orbits”. In: *Journal of Guidance, Control, and Dynamics* 40.7 (2017), pp. 1749–1768.

[25] John Lygeros e Federico Ramponi. “Lecture notes on linear system theory”. In: *Automatic Control Laboratory, ETH Zurich* (2010).

[26] Michele Maestrini, Pierluigi Di Lizia e Francesco Topputo. “Analytical Impulsive-to-Continuous Thrust Conversion in Linearized Relative Dynamics”. In: *Journal of Guidance, Control, and Dynamics* 44.4 (2021), pp. 862–871.

[27] Danylo Malyuta et al. “Advances in trajectory optimization for space vehicle control”. In: *Annual Reviews in Control* 52 (2021), pp. 282–315.

[28] C Priyant Mark e Surekha Kamath. “Review of active space debris removal methods”. In: *Space Policy* 47 (2019), pp. 194–206.

[29] F Landis Markley e John L Crassidis. *Fundamentals of spacecraft attitude determination and control*. Springer, 2014.

[30] Darren McKnight et al. “Identifying the 50 statistically-most-concerning derelict objects in LEO”. In: *Acta Astronautica* 181 (2021), pp. 282–291.

[31] MMT-9. URL: https://www.astroguard.ru.

[32] T Sasaki, Y Nakajima e T Yamamoto. “Proximity Approaches for Active Debris Removal Satellites Considering Trajectory Safety”. In: *International Symposium on Space Technology and Science*. 2019.

[33] Jürgen Telaar et al. “GNC architecture for the e. Deorbit mission”. In: *7th European Conference for Aeronautics and Space Sciences (EUCASS)*. 2017.

[34] Jacopo Ventura et al. “An inverse dynamics-based trajectory planner for autonomous docking to a tumbling target”. In: *AIAA guidance, navigation, and control conference*. 2016, p. 0876.

[35] Bong Wie. *Space Vehicle Guidance, Control and Astrodynamics*. American Institute of Aeronautics e Astronautics, Inc., 2015.

[36] David C Woffinden. “On-orbit satellite inspection: navigation and [Delta] v analysis”. Tesi di dott. Massachusetts Institute of Technology, 2004.

[37] Toru Yamamoto et al. “GNC Strategy to Capture, Stabilize and Remove Large Space Debris”. In: *1st International Orbital Debris Conference, Texas, USA*. 6109. 2019.

[38] Richard Zappulla et al. “Experiments on autonomous spacecraft rendezvous and docking using an adaptive artificial potential field approach”. In: *26th AAS/AIAA Space Flight Mechanics Meeting, Napa, CA*. 2016, pp. 4461–4478.